EMBRY-RIDDLE
Aeronautical University
SCHOLARLY COMMONS

Dissertations and Theses

12-2019

Numerical Investigation of Scaling Effects of a Ramjet-Powered Projectile

Arjun Jaishankar Vedam

NUMERICAL INVESTIGATION OF SCALING EFFECTS OF A RAMJET-POWERED PROJECTILE

A Thesis

Submitted to the Faculty

of

Embry-Riddle Aeronautical University

by

Arjun Jaishankar Vedam

In Partial Fulfillment of the

Requirements for the Degree

of

Master of Science in Aerospace Engineering

December 2019

Embry-Riddle Aeronautical University

Daytona Beach, Florida

NUMERICAL INVESTIGATION OF SCALING EFFECTS
OF A RAMJET-POWERED PROJECTILE

by

Arjun Jaishankar Vedam

This Thesis was prepared under the direction of the candidate's Thesis Committee Chair, Dr. William Engblom, Department of Aerospace Engineering, and has been approved by the members of the thesis committee. It was submitted to the Office of the Senior Vice President for Academic Affairs and Provost, and was accepted in partial fulfillment of the requirements for the degree of Master of Science in Aerospace Engineering.

THESIS COMMITTEE

Chairman, Dr. William Englblom

Member, Dr. Lakshmanan Narayanaswami

Member, Dr. Eric Perrell

Dr. Magdy S. Attia — Digitally signed by Dr. Magdy S. Attia Date: 2019.12.06 11:45:44 -05'00'

Graduate Program Coordinator
Dr. Magdy Attia

12 / 06 / 2019
Date

Dean of College of Engineering
Dr. Maj Mirmirani

12/6/19
Date

Associate Provost of Academic Support
Dr. Christopher Grant

12/6/19
Date

ACKNOWLEDGMENTS

My biggest token of gratitude goes to Dr. William Englom for his patience, willingness, guidance and support as my advisor throughout the research process. Without him, this would not have been possible.

I also want to thank my committee members, Dr. Perrell and Dr. Narayanaswami, for their continued support and participation, as well as timely advice and suggestions, when required. I would also like to thank Dr. Reda Mankbadi for his words of encouragement when things weren't going the way I expected them to. No academic achievement is accomplished without the help and support of one's fellow peers. I thank them all for assisting me in any way they could.

Last, but never least, to my parents and my sister, I thank you for putting up with prolonged communication absences, and for providing emotional and mental support from over nine thousand miles away.

TABLE OF CONTENTS

LIST OF TABLES

LIST OF FIGURES

Figure Page

SYMBOLS

A	Pre-exponential factor
b	Temperature exponent
C_D	Coefficient of Drag
C_p	Specific heat capacity
e	Internal energy
E_a	Activation energy
F	Forward thrust
F_D	Drag
F_N	Net Force
g_0	Acceleration due to gravity
I_{sp}	Specific Impulse
k	Turbulent Kinetic Energy
Pr_t	Turbulent Prandtl Number
$\mathbf{q}$	Heat flux
Re_{θ_t}	Transition Onset Momentum Thickness Reynolds Number
R_u	Universal gas constant
Δs	Minimum normal-to-wall spacing
S	Area
Sc_t	Turbulent Schmidt Number
$\mathbf{u}$	Massflow-weighted velocity
$\mathbf{V_k}$	Mass Diffusion of species k
$y+$	Dimensionless wall distance
Y_k	Mass fraction of species k
β	Conical shock angle
ε	Turbulent Dissipation Rate

γ	Intermittency
η	Combustion efficiency
η_κ	Kolmogorov scale
κ	Bulk viscosity
μ	Dynamic viscosity
μ_t	Eddy viscosity
ω	Specific Dissipation Rate
Ω_k	Rate of production of species k
ϕ	Equivalence Ratio
ρ	Mass density
τ	Viscous stress tensor
θ	Cone deflection angle

ABBREVIATIONS

AUSM	Advection Upstream Splitting Method
CAD	Computer-Aided Drawing
CFD	Computational Fluid Dynamics
DES	Detached-Eddy Simulation
EDC	Eddy-Dissipation Concept
EDM	Eddy-Dissipation Model
FR	Finite-Rate/Laminar Chemistry
FR-EDM	Finite-rate/Eddy-Dissipation Model
LES	Large-Eddy Simulation
RANS	Reynolds-Averaged Navier Stokes
SBLI	Shockwave-Boundary Layer Interaction
SST	Shear Stress Transport
SST-Tr	Transition Shear Stress Transport
UAV	Unmanned Aerial Vehicle
WMLES	Wall-Modeled LES

ABSTRACT

Ramjet flowpath miniaturization is a potentially useful technology for integration into munitions to increase range, accuracy, and lethality. The emphasis of this effort is to numerically characterize the performance of a miniature hydrogen-fueled and ethylene-fueled ramjet flowpath during Mach 3 and Mach 3.5 sea-level flight. The effect of geometric scale on ramjet performance is evaluated using high-fidelity RANS CFD models. Sensitivity to nonequilibrium laminar and turbulence-limited chemistry, and transitional turbulence treatments are evaluated. The physical sources of small scale performance limitations are identified for both fuel types. Finally, flowpath integration for small-scale applications is briefly addressed.

1. Introduction

1.1 Background and Motivation

Advancements in scalable, adaptable munition systems are being sought by the United States Army (USArmy, 2017). Whether being fired from UAVs or hand-held guns, there is interest in development of faster, more lethal, more accurate, and longer range munitions. Drones with the ability to have guns mounted and fired from them have been developed by Duke Robotics Inc., as shown in Figure 1.1. These devices ensure the safety of soldiers when used as a remotely operated device, and offer a quick and efficient form of handling potentially dangerous situations (Duke-Robotics, 2017).

Figure 1.1 TIKAD Drone.

Traditional artillery shells are propelled using explosive gunpowder and percussion caps, and are not self-propelled. The velocity of the unpropelled shell velocity decreases during the subsequent flight. By integrating a fuel and oxidizer within the artillery shell to allow self-propulsion, there is a possibility for maintaining velocity during flight. Raytheon has developed the Pike munition system, shown in Figure 1.2, which integrates a rocket motor in the artillery shell of a hand-held gun to propel the projectile at increased velocities (Raytheon, 2015). A drawback of this type of bullet is the need to carry oxidizer on board which would limit performance due to increased weight.

Figure 1.2 Rocket-powered Pike munition.

To overcome limitations of rocket-powered munitions, experiments have been conducted to test feasibility of solid-fuel ramjet (SFRJ) motors (Dionisio and Stockenstrm, 2001). Ground tests indicate a specific impulse (I_{sp}) value of 1111 seconds with SFRJ-powered munitions (Stockenstrm, 2001). Nordic Ammunition Company (NAMMO) has reported successful integration of SFRJ motors in artillery shells (Figure 1.3), and plan to begin flight tests in 2020 (Judson, 2018). Although performance of SFRJ demonstrates a vast improvement over the fuel efficiency of rocket motors, there is no available evidence that it would be efficient at much smaller geometric scales, on the order of a few inches in length. SFRJ projectiles at miniature scales could prove difficult to implement, given the relatively short time frame for vaporization, mixing, and ignition of solid fuel grain. A ramjet projectile using gaseous fuels like hydrogen (H_2) and ethylene (C_2H_4), or liquid propellants like JP-7, may be a valuable alternative at smaller geometric scales, as the reduced mass might provide higher thrust and better efficiency.

Figure 1.3 SFRJ developed by NAMMO, on display at Eurosatory Expo, 2018.

1.2 Ramjet Fundamentals

The concept of a ramjet engine was proposed by Albert Fono and Rene Lorin in the early 20^{th} century (Gilreath, 1990). A ramjet is a type of air-breathing engine that utilizes dynamic air pressure created by the moving object to increase pressure levels inside the engine without the use of moving parts, i.e., “ram effect.” A basic ramjet engine consists of three distinct regions, as shown in Figure 1.4:

1. **Inlet:** Also known as the diffuser, the inlet compresses and diffuses incoming supersonic air to subsonic speeds through a system of oblique and normal shocks.

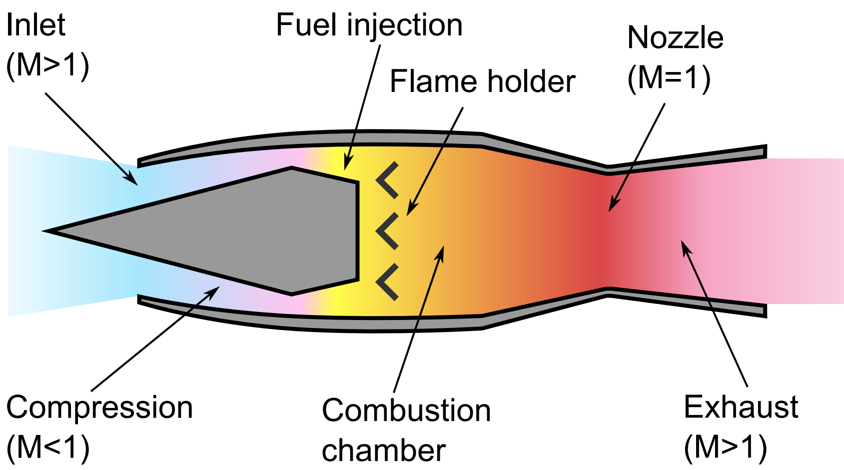

Figure 1.4 Schematic of a Ramjet Engine.

2. **Combustion chamber:** Fuel in solid, liquid, or gaseous state is mixed with the compressed air at subsonic speeds and ignited. Sufficiently high levels of temperature and turbulence are required to obtain high efficiency combustion.

3. **Nozzle:** Expands the burnt fuel-air mixture into the atmosphere at increased velocity. At small geometric scales, it is expected that the nozzle also acts as an after-burner due to the reduced mixing time in the combustor.

1.3 Literature Review

1.3.1 Ramjet Experimental Data

Available experimental data for small-scale ramjet performance is scarce possibly due to security restrictions, as well as limited availability of test facilities. Published data for a Hydrogen-fueled Ramjet indicates a high I_{sp} of 3600s, and total thrust 2200N for 7.6m long flowpath (Frolov et al., 2017). A solid-fueled 155mm ramjet projectile with self-propelling capabilities has been tested (Dionisio and Stockenstrm, 2001) and numerically validated (Stockenstrm, 2001), with performance data indicating an I_{sp} of

1111s. Although the ramjet flowpath configuration is unavailable for either of these experimental and numerical tests, the results do provide a target I_{sp} when evaluating the performance of the ramjet flowpath developed in this thesis.

Ferguson (2003) developed a structurally robust projectile that could handle aerodynamic loads at $M_\infty = 4.0$. A non-reacting numerical simulation was also performed in their work, and suggestions were made to improve CFD calculations using reacting flows.

1.3.2 CFD of Ram/Scramjet Combustion

The non-equilibrium chemical nature of high-speed combustion problems presents a major challenge, especially when validating existing CFD codes and numerical models. Edwards et. al. (2010) produced an accurate LES study of the Burrows-Kurkov H_2-air supersonic combustor experiment (Burrows and Kurkov, 1971), using a low-dissipation piecewise parabolic advection scheme that was able to capture small-scale turbulent eddies. Engblom et. al. (2005) validated high-fidelity RANS analysis on the same high-speed combustion experiment. Borghi et. al. (2012) validated RANS analysis of a dual-mode ramjet using a simplified ethylene-methane-air reaction model, using a combination of finite-rate chemical kinetics and a turbulence mixing limitation. (Vyas et al., 2012) validated a RANS model of a dual-mode ramjet using a detailed H_2-air chemical kinetics model.

Chen et. al. (2015) presented different fuel injector location configurations for a miniature ramjet combustor with a cavity. Using a methane-air one-step chemical mechanism, seven different injection locations were examined using ANSYS Fluent. The authors showed that injecting fuel upstream of the cavity had little effect on the overall performance of the miniature combustor with respect to the combustion efficiency, and injecting fuel directly into a cavity failed to produce a sustained pilot flame due to the fuel-rich nature within the cavity.

1.3.3 Turbulence Model Relevant to Ramjets

A four-equation transition RANS model is used in this thesis, with the expectations that it will accurately capture laminar-to-turbulent transition at smaller geometric scales. Langtry and Menter (2006) proposed a turbulence model coupled with the original Shear-Stress Transport (SST) turbulence model (Menter, 1994) that could accurately predict the transition from laminar to turbulent flow. It is a four-equation model that couples the original $k-\omega$ variables with two new variables: γ and $Re_{\theta t}$. Menter's four equation SST transitional model has been validated for moderate Reynolds number low-speed flows (Granizo et al., 2017), (Willems et al., 2018). Using this transition model, You et. al. (2012) showed that direct application of this model accurately predicted the transition in high-speed flows, and a 30% over-estimated heat flux in shock-impingement cases. Since the main concern in this thesis is the subsonic combustion in a small-scale combustor in which the flow is expected to predominantly laminar, this model is deemed appropriate.

It should, however, be noted that Georgiadis et. al. (2011) demonstrated the limitations within a RANS framework, especially in ramjet mode, citing the inability of two-equation RANS models to accurately predict turbulent transition and shock-boundary layer interaction at compression corners of air-breathing intakes. LES is offered as a useful alternative but comments are made about the limitations of LES, with respect to the enormous computational cost and inaccuracies predicting turbulent mixing and turbulent-chemistry interactions.

1.3.4 Turbulent-Chemistry Interactions for Ramjet Flows

The chemical interactions that take place in the combustor are numerically evaluated using a commercial CFD code, ANSYS Fluent, which provides four chemical interaction models (ANSYS-Inc., 2019a):

1. Finite-rate chemistry (FR, no turbulent-chemistry interaction).
2. Finite-rate/Eddy-Dissipation Model (FR-EDM).
3. Eddy-Dissipation Model (EDM).
4. Eddy-Dissipation Concept (EDC).

It should be pointed out that ANSYS' definition of EDC differs from the definition of EDC shown in much of the relevant literature, e.g., (Chen et al., 2015), (Edwards and Fulton, 2015), and (Borghi et al., 2014). This literature defines EDC in the same way that ANSYS defines the EDM interaction model, in which the turbulent interaction of fuel and air is governed by the large-eddy mixing time scale, k/ε, first proposed by Magnussen and Hjertager (1976). ANSYS' EDC model assumes the reaction occurs in the fine scales, or the smallest turbulent structures, which can be used when the assumption of fast chemistry is invalid (Magnussen, 1981), and is therefore not used to evaluate performance sensitivity. A numerical comparison of meso-scale combustion using the EDC and FR models is performed in (Minotti and Bruno, 2011), which suggests that EDC performs better when using detailed chemical mechanisms, i.e. multi-step reactions. Only the first three interaction models (FR, FR-EDM, and EDM) are investigated in this thesis.

1.4 Objectives

The objectives of this thesis are as follows:

- Develop a simplified, scalable ramjet flowpath configuration.
- Numerically evaluate performance of ramjet flowpath at different geometric scales with high-fidelity CFD models, using two different fuels: H_2 and C_2H_4,
- Determine physical cause of performance limitations at the smallest scales.
- Evaluate the sensitivity of performance to the treatment of turbulent chemical interactions using finite-rate chemistry, the Eddy-Dissipation Model (EDM), and a combination of finite-rate and EDM.

2. Numerical Methodology

This chapter presents a detailed description of the ramjet flowpath design, performance metrics, computational grid and boundary conditions, and the numerical schemes and models, including the treatment of chemical kinetics.

2.1 Ramjet flowpath design

An archetype ramjet flowpath configuration is developed to operate efficiently at Mach 3, at sea level conditions (see Table 2.1). It should be recognized that the ramjet flowpath and fuel injector configuration are simple and non-optimal, but expected to provide relevant information on scalability effects.

Table 2.1

Freestream Operating Conditions

Property	Value
Static Pressure (P_∞)	101325 Pa
Static Temperature (T_∞)	300 K
Mach number (M_∞)	3, 3.5

2.1.1 Inlet

The inlet (or diffuser) section of the ramjet is configured using one-dimensional compressible flow equations (Anderson, 1982). The first parameter considered is the deflection half-angle (θ) of the inlet spike. The conical spike half-angle is chosen to reduce the overall drag of the engine, aid in stagnation pressure recovery, and prevent unstart. A simple system of two-shocks is expected to be sufficient for the inlet, with a leading conical shock and a terminal normal shock to achieve desired compression. Based on analytical tests done by Ferguson (2003), $\theta = 17.5°$ is determined to have the best stagnation pressure recovery for a ramjet at Mach 3, as depicted in Figure 2.2. The stagnation pressure recovery across the two-shock system is calculated using Equation 2.1, where P_{0c} is the freestream stagnation pressure, A_c and A_t are known geometric parameters, and 4.235 is a constant determined using the isentropic *Area-Mach number* equation from Anderson (1982). The cowl lip is constrained one unit length downstream of the cone tip, as shown in Figure 2.1, so that the leading oblique shock hits the cowl lip. The exit area of the diffuser (A_d) is evaluated using Equation 2.2 for subsonic flow at $M_d = 0.3$. For $M_d \leq 0.25$, A_d would be greater than A_c, which is undesirable from an integration standpoint since it could increase the overall diameter of the munition.

$$P_{0c} = 4.235 * \frac{A_t P_{0t}}{A_c} \tag{2.1}$$

$$A_d = A_t \left[\left(\frac{\gamma+1}{2} \right)^{\frac{-\gamma+1}{2(\gamma-1)}} \right] \left[\frac{\left(1 + \frac{\gamma-1}{2} M^2\right)^{\frac{\gamma+1}{2(\gamma-1)}}}{M} \right] \tag{2.2}$$

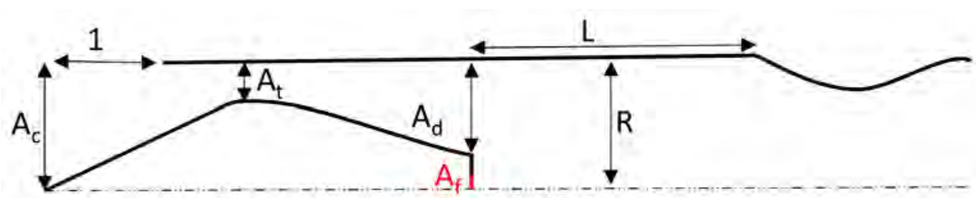

Figure 2.1 Baseline ramjet geometry parameters

2.1.2 Combustor and Fuel Injector

The combustor is a straight axisymmetric section where stored fuel is injected, mixed with the incoming air and ignited. Ideal thrust-to-weight ratio is achieved at L/R = 6

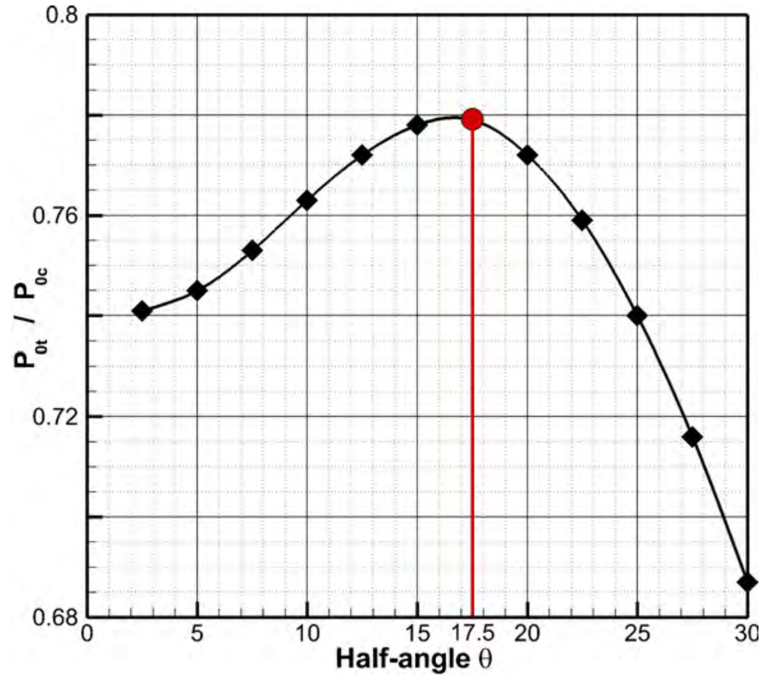

Figure 2.2 Stagnation Pressure Recovery across the two-shock system (Ferguson, 2003).

(Chen et al., 2015), where L and R are the length and the radius of the combustor, respectively. Design restrictions limited the flow Mach number at the combustor entrance (A_d) to as low as Mach 0.3.

The fuel injector exit plane, shown in red in Figure 2.1, is placed along the centerline, aft of the diffuser section. Fuel is injected at sonic velocity in the axial direction into the low-speed flame holding region. This generates a shear layer near the fuel injection site and promotes turbulent mixing and ignition. The ratio of injector area (A_f) to capture area (A_c) is maintained throughout the geometric scaling process:

$(A_f/A_c)_{H_2-air} = 3.086E-02$ and $(A_f/A_c)_{C_2H_4-air} = 2.623E-02$

High-speed combustion chambers normally utilize cavities that hold pilot flames and ignite the fuel-air mixture. However, according to Chen et. al. (2015), a cavity is deemed unnecessary at small geometric scales. Therefore, a cavity is not used and fuel is injected directly into the combustor.

2.1.3 Nozzle

The nozzle is configured to isentropically expand to axial flow at the exit. This is done without increasing the overall diameter of the ramjet flowpath, and therefore minimizing flowpath drag.

2.2 Performance Metrics

Four parameters are calculated to measure performance of the ramjet at different geometric scales. To define these parameters, a representation of the control volume, depicted in red, is shown in Figure 2.3. This control volume accounts only for the mass flow captured within the cowl body, labeled station *i*.

Figure 2.3 Control Volume for Performance Calculations.

1. **Thrust (F):** Thrust is computed as the difference in mass flow-averaged axial momentum flux and mass flow-averaged pressure forces across the control volume:

$$F = \dot{m}_e u_e - \dot{m}_i u_i + A_e(P_e - P_\infty) \tag{2.3}$$

2. **Specific Impulse (I_{sp}):** It is a measure of the thrust produced by the engine per unit weight of fuel injected:

$$I_{sp} = \frac{F}{\dot{m}_f g_0} \tag{2.4}$$

3. **Net Force (F_N):** It is measured using a summation of the wall forces, both pressure and frictional. It can also calculated as the difference in mass flow-averaged momentum flux and mass flow-averaged pressure forces across the entire domain (see Equation 2.5). Note that the difference between the thrust and net force is the skin friction drag force along the upper external surface of the flowpath cowl and the external portion of the conical centerbody.

$$F_N = \dot{m}_e u_e + \dot{m}_{e0} u_{e0} - \dot{m}_\infty u_\infty + A_e P_e + A_{e0} P_{e0} - A_\infty P_\infty \tag{2.5}$$

4. **Combustion efficiency (η_c):** Efficiency is defined in this work as the ratio of mass fraction of a product species at the nozzle exit to the theoretical mass fraction of the product in the exhaust assuming all the injected fuel is burned completely. For H_2-air and C_2H_4-air, it is calculated using Equations 2.6 and 2.7, respectively, for ϕ-adjusted reactions.

$$\eta_{H_2-air} = \frac{Y_{H_2O}}{0.081} * 100\% \tag{2.6}$$

$$\eta_{C_2H_4-air} = \frac{Y_{CO_2}}{0.0422} * 100\% \tag{2.7}$$

The effects of geometric scale on is inferred by performing calculations of these metrics at nine different geometric scales. The scales ranged from 1:1 (full-scale 8.1m flowpath length) to 1:256 (3cm flowpath length). All nine scales are shown in Table 2.2.

Table 2.2

Matrix of Cases for Scale Sensitivity Study

Scale factor	**Length (m)**	**Injection diameter (mm)**	
		H_2**-air**	C_2H_4**-air**
1 : 1	8.10E+00	32	27.2
1 : 2	4.05E+00	16	13.6
1 : 4	2.02E+00	8	6.8
1 : 8	1.01E+00	4	3.4
1 : 16	5.06E-01	2	1.7
1 : 32	2.53E-01	1	0.85
1 : 64	1.26E-01	0.5	0.425
1 : 128	6.33E-02	0.25	0.2125
1 : 256	3.16E-02	0.125	0.10625

2.3 Computational Grid and Boundary Conditions

2.3.1 2-D Computational Domain

The 2D computational grid is shown in Figure 2.4. A two-zone grid is used: an ‘inner’ combustor and nozzle section shown in red, and an ‘outer’ section shown in blue. A grid independence study is performed for the full-scale baseline and the 1:128 scale geometries, each with a coarse (26,000 cells) grid and a fine (104,000 cells) grid. The fine grid is constructed by doubling grid resolution in both x and y computational directions. Results for the full-scale indicate that there is a small 1.6% difference in F and I_{sp}, as shown in Figure 2.5(a). The study conducted for the 1:128 scale show that the results change by 0.29% (see Figure 2.5(b)). Consequently, since the fine grid does not significantly improve accuracy, the coarse grid has been used in the subsequent investigation for computational efficiency. A dimensionless wall distance value (y+) of 2 is maintained to capture boundary layer along the walls for all scales, which results in $\Delta s = 1E-06m$ for the 1:1, and $\Delta s = 7.8E-09m$ for the 1:128 scale.

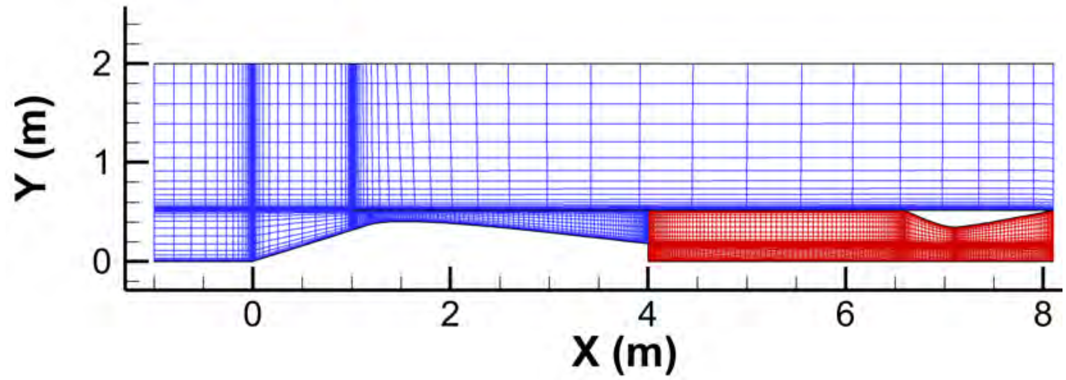

Figure 2.4 Coarse computational grid.

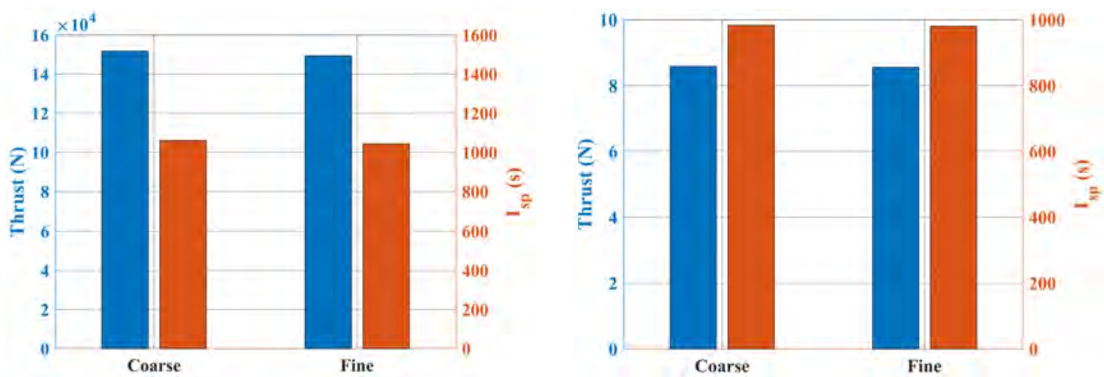

(a) Baseline. (b) 1:128 scale.

Figure 2.5 Grid independence study for (a) Baseline and (b) Small-scale 1:128.

2.3.2 3-D Computational Domain

The 2-D calculations provide a preliminary investigation to the effects of scale. However, turbulence cannot be accurately characterized using 2-D simulations. Therefore, to accurately predict turbulent effects along the flowpath, a three-dimensional grid is developed. The grid is a 30° pie-section consisting of 1,528,160 cells, revolved from the 2-D grid described above, except for the region immediately downstream of the injection port. The 2-D grid is revolved using 41 points along the 30° circumferential arc. Isometric projection of the grid is shown in Figure 2.6.

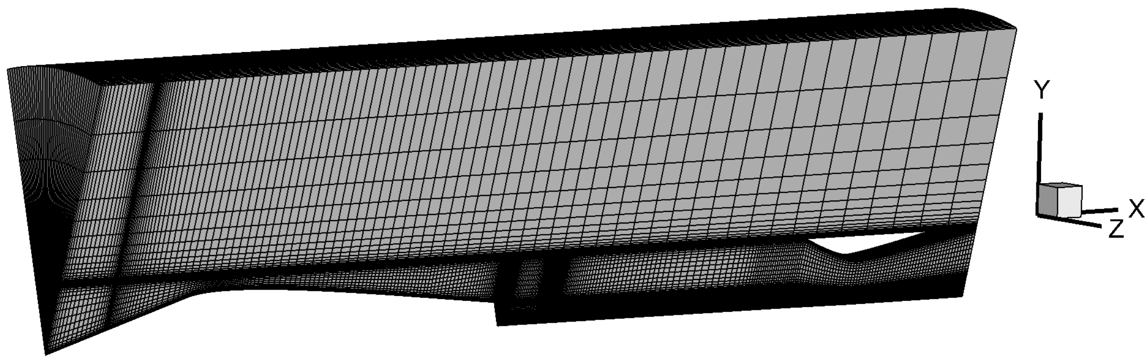

Figure 2.6 Pie section of three-dimensional grid that consists of structured and unstructured blocks.

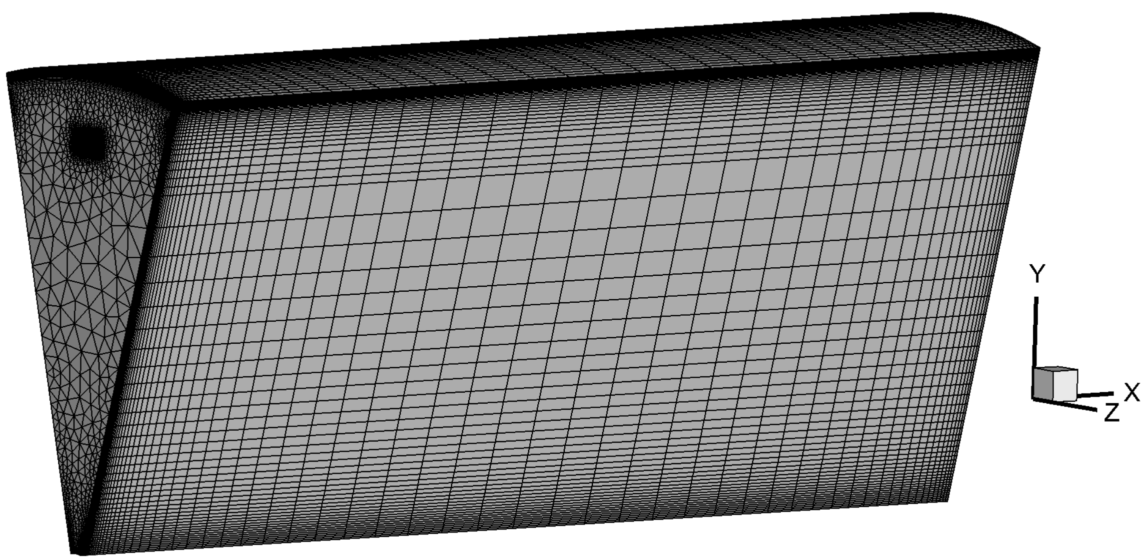

Figure 2.7 Unstructured prism block downstream of fuel injection port.

The region downstream of the injector is treated using an unstructured block consisting of triangular prisms concentrated near the fuel injection port, as shown in Figure 2.7. The fine grid near injection site allows for improved evaluation of injector jet turbulence than in the 2-D grid. Wall spacings are determined such that y+ at any point along the walls doesn't exceed a value of 5. Simulations are performed only for C_2H_4-air, and only at the small 1:64 geometric scale, as that is the size of most interest to develop a munition. The 3-D pie-section potentially provides a more realistic characterization of the injected flow and resulting turbulence levels within the ramjet flowpath than the 2-D model (Ouellette, 2012).

2.3.3 Boundary Conditions

The boundary conditions for the computational grid is shown in Figure 2.8, and values at each boundary are illustrated in Table 2.3. Each boundary condition is discussed below.

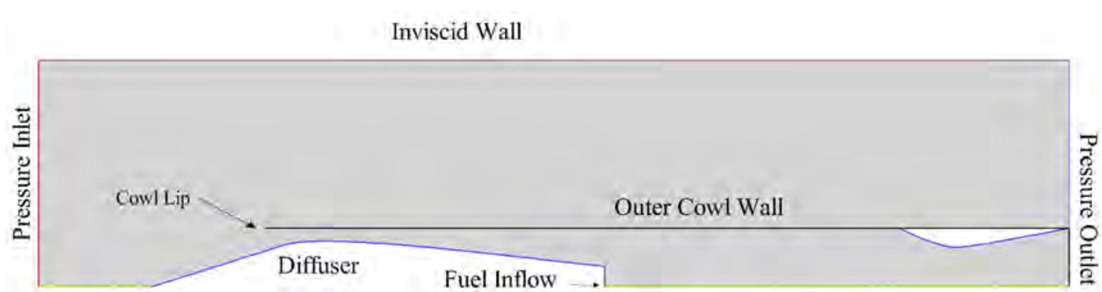

Figure 2.8 Boundary Conditions

- The inlet of the entire domain is a *Velocity Inlet*, with the supersonic velocity, the static temperature and the static pressure maintained constant. For C_2H_4 the free-stream conditions are set at Mach 3.5, since it was determined the stagnation temperature for Mach 3 flow was not sufficient to auto-ignite the fuel in the combustor.

- The fuel injector exit is a *Pressure Inlet* for the 2-D cases. The fuel inflow stagnation pressure is maintained high enough ($\geq 10MPa$) that the the rise in stagnation pressure on initiation of combustion, due to the fixed-geometry nozzle downstream of the combustor, doesn't result in reversed flow through the fuel inlet. For the 3-D cases, the fuel inlet is a *Velocity Inlet*, where sonic velocity is maintained constant at a pressure that is slightly higher ($= 4MPa$) than that of the static pressure rise due to combustion. Stagnation temperature is typical sea-level value at 300K. Injector exit values are indicated in Table 2.3.

- The ramjet body is made of adiabatic, no-slip walls. Flight duration for the munition is assumed to be short enough that the walls do not have sufficient time to heat significantly.

- The upper wall of the domain is modeled as an inviscid wall to prevent loss of mass flow at the domain outlet.

- The lower boundary for the 2-D grid is the axis of symmetry.

- For the 3-D grid, the lower boundary is an inviscid wall, and the walls of the pie section are symmetry planes.

2.4 Numerical Schemes and Models

The coupled-implicit RANS equations are solved simultaneously using the density-based solver in ANSYS Fluent (ANSYS-Inc., 2019b). The inviscid flux scheme chosen is the AUSM scheme, presented in (Liou and Steffen Jr., 1993), with second-order upwind spatial accuracy and local time-stepping. The courant number (Courant et al.,

Table 2.3

Initial Conditions

Air Inlet ($M_\infty = 3$)	U_∞	1057 m/s
	P_∞	101325 Pa
	T_∞	300 K
	Y_{N_2}	0.79
	Y_{O_2}	0.21
Air Inlet ($M_\infty = 3.5$)	U_∞	1215 m/s
	P_∞	101325 Pa
	T_∞	300 K
	Y_{N_2}	0.79
	Y_{O_2}	0.21
H_2 Pressure Inlet ($M_{inj} = 1$, $\phi = 0.2$)	$P_{0_{H_2}}$	11.37 MPa
	$T_{0_{H_2}}$	300 K
	$Y_{f_{H_2}}$	1
2-D C_2H_4 Pressure Inlet ($M_{inj} = 1$, $\phi = 0.2$)	$P_{0_{C_2H_4}}$	10.77 MPa
	$T_{0_{C_2H_4}}$	300 K
	$Y_{f_{C_2H_4}}$	1
3-D C_2H_4 Velocity Inlet ($M_{inj} = 1$, $\phi = 0.2$)	$U_{C_2H_4}$	332 m/s
	$T_{C_2H_4}$	267 K
	$Y_{f_{C_2H_4}}$	1

1956), which relates the time step size, cell size, and velocity, is set as 1 to drive the solution towards steady-state.

The fully turbulent SST model (Menter, 1994) has been validated for high-speed reacting flows (Georgiadis et al., 2011) (Engblom et al., 2005). It is a robust 2-equation model for μ_t that combines the $k-\omega$ model near the walls and the $k-\varepsilon$ model in the free-shear flow regions, with a blending function that transitions between the two. At the smaller geometric scales, it is expected that the onset of turbulence is delayed further downstream along the walls of the ramjet diffuser, and it is crucial to the transition from laminar to turbulent flow for prediction of mixing and combustion.

An extension to the SST turbulence model was proposed by adding two transport equations used to predict the transition from laminar to turbulent boundary layer (Menter et al., 2006). Of the two new turbulence variables that arise in the model, the first variable γ predicts the onset of turbulence, and the second variable Re_{θ_t} estimates the length of transition using empirical correlations. γ is set to 0 in the freestream and fuel injector, assuming that there is no onset of turbulence at the respective inlets. Re_{θ_t} is a function of the turbulent intensity in the freestream, and is required by the γ equation inside the boundary layer regions of the flow. Essentially, Re_{θ_t} is a transported scalar that models the local turbulent transition at every point in the flow-field. Turbulent parameters for fuel and air inflow boundaries are specified in Table 2.4. The values for k and ω are selected based on a previous study (Liou and Shih, 1996) and numerical investigation of the fuel injection flowpath presented in the Results chapter.

Table 2.4

Turbulent Parameters for 2-D Inlet Boundary Conditions

Fuel Inlet	γ	0
	k	1000 m^2/s^2
	ω	1.00E+07 s^{-1}
Air Inlet	γ	0
	k	1 m^2/s^2
	ω	1 s^{-1}

The SST-transition (SST-Tr) model, developed and validated for subsonic and transonic regimes (Langtry and Menter, 2009), has been used in the present study. For hypersonic flows, (Frauholz et al., 2015) showed that the separation bubble in scramjet intakes can be accurately predicted using this model. When combined with the Reynolds

Stress Model, the transition model outperformed the fully turbulent SST computations for a variety of intakes, showing better predictions for pressure and heat loads on the intake. Although the transition is predicted well for hypersonic flows, it has been suggested that improvements are required within the model since it over-predicts heat flux by nearly 30% in shock-impingement cases (You et al., 2012). The transition model was deemed appropriate for the current study despite this drawback, since the cases considered in this thesis deal with the separation bubble in the intake, and largely subsonic flow within the combustor section.

Two fuels are evaluated: H_2 and C_2H_4. Global chemical kinetics models are selected for the laminar finite-rate reactions for each fuel. H_2-air is a 4-species, single reaction model, and C_2H_4-air is a 5-species, single reaction model. Values for the Arrhenius reaction rates are given in Table 2.5 (ANSYS-Inc., 2019b). A is the pre-exponential factor, b is the temperature exponent and E_a/R_u is the activation temperature. The forward reaction rate constant is calculated as $k = AT^b exp^{\frac{E_a}{R_u T}}$, where R_u is the universal gas constant and units of the activation temperature and the pre-exponential factor are K and $m^3/kgmol$-s, respectively.

Table 2.5

Global kinetics Arrhenius reaction rates for H_2-air and C_2H_4-air reactions

Reaction	**A**	**b**	E_a/R_u
$H_2 + 0.5O_2 + 3.76N_2 \longrightarrow 2H_2O + 3.76N_2$	9.87e+08	0	3726
$C_2H_4 + 14.28(0.21O_2 + 0.79N_2) \longrightarrow 2CO_2 + 2H_2O + 3.76N_2$	1.125e+10	0	15,098

Unstart of a ramjet engine is a phenomenon in which the normal shock formed in the nozzle moves upstream into the diffuser and 'chokes' off the flow entering the inlet throat due to insufficient intake compression, leading to a sudden reduction in performance. It is usually caused by an increase in stagnation pressure downstream of the inlet throat at higher equivalence ratios (ϕ). To evaluate the sensitivity of the flowpath to ϕ, a range of values of ϕ is utilized for analysis, starting from 0.1 with increments of 0.05. It is observed that the ramjet tended to unstart at $\phi \geq 0.25$. Therefore, ϕ is restricted to a value of 0.2 in this thesis. This sensitivity to ϕ is presented in the results chapter.

The reactions are modeled using three chemical interaction schemes: (i) laminar finite-rate chemistry (FR); (ii) turbulence-limited Eddy-Dissipation Model (EDM); and (iii) a combination of EDM and laminar finite-rate chemistry (FR-EDM), in which the minimum rate is used to limit the reaction. EDM is often referred to as Eddy-Dissipation Concept (EDC) like in (Edwards and Fulton, 2015) and (Borghi et al., 2014). The model was first proposed by (Magnussen and Hjertager, 1977). It accounts for turbulent mixing of the fuel and oxidizer at the smallest turbulent Kolmogorov scales, and puts an additional turublence limit on the Arrhenius reaction rates. ANSYS Fluent's EDC model utilizes an extended equation that accounts for detailed reaction mechanisms (Magnussen, 1981), and is not used in this work.

The net production rate of the species for a given reaction in the EDM mechanism is given by the smaller limiting value of equation 2.8 and 2.9, where: i and j indicate species; r indicates the reaction; $\nu'_{i,r}$ is the stoichiometric coefficient of i in r; Y_P is the mass fraction of the product species; Y_R is the mass fraction of reactant species; k/ε is the large-eddy mixing time scale; and $A = 4.0$ *and* $B = 1e{+}10$ are empirical constants. When turbulence is present, i.e. $k/\varepsilon > 0$, the reaction proceeds and an ignition source is not required to initiate combustion. For non-premixed flames, presence of turbulence assumes “mixed is burned,” i.e. complete fuel-air mixing at every turbulent scale burns without an ignition source. The empirical constant B controls the presence of “hot products” in the reaction zones, and it is set large enough to ensure that the lack of presence of hot products does not limit reaction rates.

$$R_{i,r} = \nu'_{i,r} M_{w,i} A \rho \frac{\varepsilon}{k} \min_{R} \left(\frac{Y_R}{\nu'_{i,r} M_{w,i}} \right) \tag{2.8}$$

$$R_{i,r} = \nu'_{i,r} M_{w,i} A B \rho \frac{\varepsilon}{k} \frac{\sum_P Y_P}{\sum_j \nu''_{j,r} M_{w,j}} \tag{2.9}$$

Thermodynamic properties are calculated in a typical manner for reacting flows. Specific heat capacity (C_p) is calculated using available curve fits from (McBride et al., 1993), assuming thermodynamic equilibrium, using a three-coefficient formula as in Equation 2.10, to solve for dynamic viscosity μ (Sutherland, 1893). Values and definitions for each coefficient is given in (ANSYS-Inc., 2019a).

$$\mu = \mu_0 \left(\frac{T}{T_0} \right)^{3/2} \frac{T_0 + S}{T + S} \tag{2.10}$$

Thermal conductivity is solved using kinetic theory, as in equation 2.11 (ANSYS-Inc., 2019a).

$$k = \frac{15}{4} \frac{R_u}{M_W} \mu \left[\frac{4}{15} \frac{C_p M_W}{R_u} + \frac{1}{3} \right] \tag{2.11}$$

Turbulent Prandtl number (Pr_t) is the ratio of turbulent momentum transfer to turbulent heat transfer. Turbulent Schmidt number (Sc_t) is the ratio of turbulent momentum transfer to turbulent mass transfer. For high speed combustion problems, typical values are Pr_t = 0.7 and Sc_t = 0.5 (Edwards et al., 2010). High-speed combustion is highly sensitive to Sc_t and small changes in the value could either lead to unstart or flame-out conditions (Georgiadis et al., 2014). Pr_t, on the other hand, doesn't have as much of a pronounced effect, as shown by Engblom et. al. (2005).

2.4.1 Large Eddy Simulations

To maintain the isotropic nature for an LES grid within the 30-degree pie section, a simple calculation was carried out to determine the total number of cells across x-, y-, and z-directions. It is found that to accurately capture boundary layer while maintaining y+ of 10:1:10 in the x:y:z directions respectively, a grid size of more than 200-million cells is required. An attempt to evaluate the computational expense of an LES simulation at small geometric scales based on Kolmogorov scale considerations is described in the results section.

3. Results and Discussion

2-D and 3-D simulations are performed on ERAU's Vega supercomputer. The 2-D simulations used 2 nodes and 72 cores, and the average simulation time for 100,000 iterations on the 2D grid was 2 hours with chemical reactions. For the 3D grid, the average simulation time for 100,000 iterations on 4 nodes and 144 cores was 35 hours. Convergence is obtained when the solver shows residual drop of at least 3 orders of magnitude for all RANS equations, and nozzle exit mass flow and mass flow-averaged velocity converge to within .01%.

3.1 Sensitivity to Equivalence Ratio

Preliminary set of results, such as shown in Figure 3.1, demonstrate the unstart phenomenon for higher values of ϕ using hydrogen as fuel. The steady state pressure contours for increasing ϕ from 0.2 to 0.25 are displayed. In the geometric 1:1 scale for H_2-air, the pressure rise in the combustion chamber for ϕ of 0.2 is sufficiently handled by the intake compression. A steady increase to ϕ of 0.25 results in an unstart in which the normal shock is pushed out of the internal flowpath and chokes the inlet, causing a subsequent pressure drop within the combustor. At this point, even with the reactions turned off, the normal shock is never again fully swallowed by the diffuser throat, confirming that the engine has fully unstarted. Consequently, to mitigate potential for unstart, all cases considered herein possess $\phi = 0.2$, for both H_2 and C_2H_4 fuels.

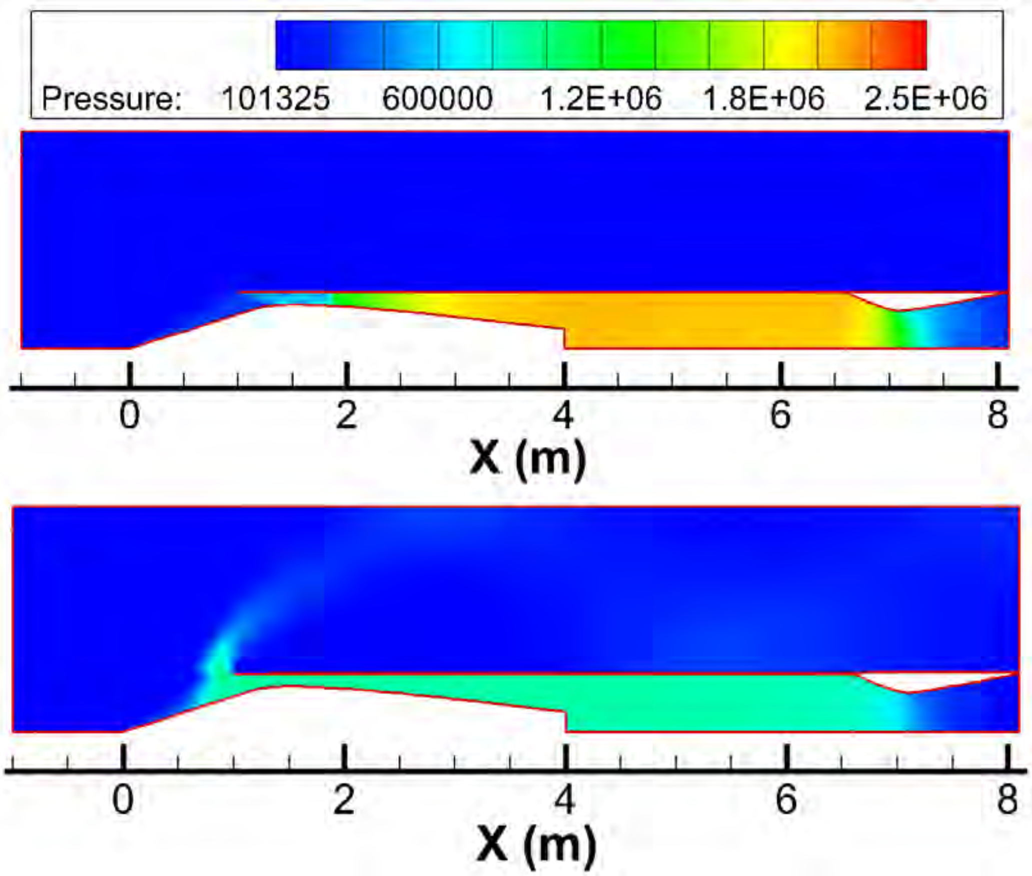

Figure 3.1 Sensitivity of flowpath to $\phi = 0.2$ (top) and $\phi = 0.25$ (bottom).

3.2 Fuel Injection Turbulent Parameters

To estimate fuel inflow turbulence in a small scale injector, a separate study of the fuel injector flowpath is conducted.

The sonic fuel injector is set up as a 2-D axisymmetric flowpath with a short subsonic section at $M = 0.3$ leading up to a nozzle that accelerates the flow to $M = 1$, followed by a long sonic section to develop a turbulent boundary layer. The inflow boundary conditions for the CFD calculation are shown in Table 3.1, assuming isentropic flow throughout the injector, Re_D of the flow at the injector outlet is 1.056E+07.

Table 3.1

Inflow Conditions for Fuel Injector

Pressure Inlet ($M_{in} = 0.3$)	P_{0in}	4 MPa
	T_{0in}	300 K
	$Y_{C_2H_4}$	1
	k	1 m^2/s^2
	ω	1 s^{-1}
	γ	0

Contours of turbulent variables, k and ω are plotted in Figures 3.2 and 3.3, respectively, showing the development of turbulence in the injector pipe. Using data from this study, and from previous studies of turbulent flow in a tunnel at transonic speeds (Liou and Shih, 1996), fuel is injected and evaluated for sensitivity to inflow k at two different levels of k: 100 m^2/s^2 and 1000 m^2/s^2; at constant ω = 1.0E+07 s^{-1}. This is expected to provide a clear picture of the dependence of fuel-air mixing and combustion on turbulent fuel inflow, and offers preliminary insight to dependence of mixture ignition over a realistic range of inflow turbulence. Range of k levels at the injector exit matches well with previous experiments and CFD data shown by Liou and Shih (1996) for transonic turbulent flow at high Reynolds numbers.

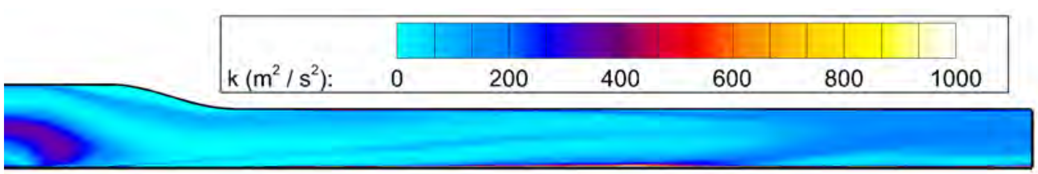

Figure 3.2 Development of k in the injector.

To confirm that the flow through small geometric scale injectors is turbulent, an analytical calculation is carried out for expected Reynolds number in the injector pipe. A

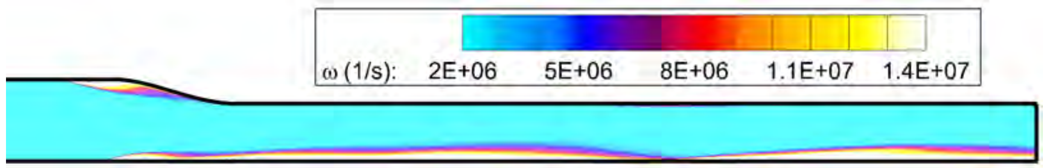

Figure 3.3 Development of ω in the injector.

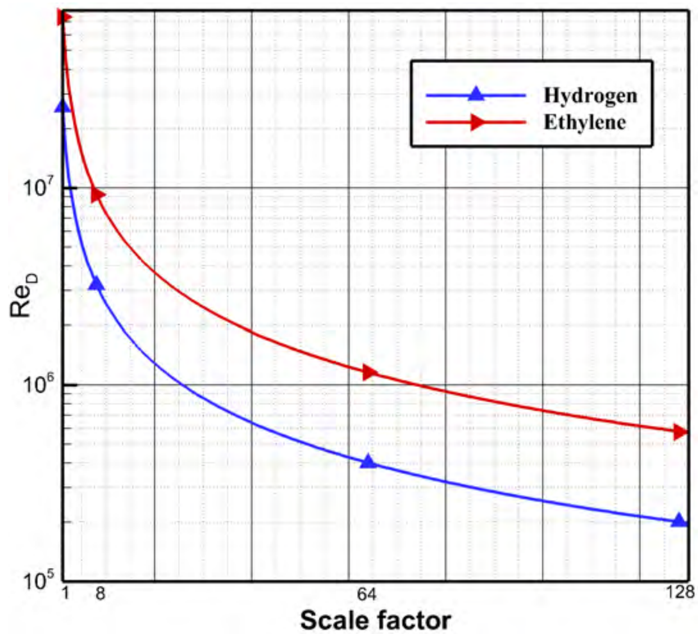

Figure 3.4 Reynolds number vs scale factor for C_2H_4 and H_2 fuels.

plot of Re_D vs scale for different injector sizes and H_2 and C_2H_4 fuels is plotted in Figure 3.4, where Re_D is calculated using the diameter of the fuel injector, dynamic viscosity, and sonic velocity of the pressurized fuel, as in equation 3.1. Flow in a pipe is considered turbulent at $Re_D > 4000$, and the analytical and numerical solutions indicate that the fuel inflow should be turbulent at the injected pressure and temperature.

$$Re_D = \frac{\rho_{inj} u_{inj} D}{\mu_{fuel}} \tag{3.1}$$

3.3 Geometric Scaling (2D)

This section analyses the effects of geometric scale on the performance metrics described in Chapter 2 for both hydrogen and ethylene fueled 2-D cases.

3.3.1 H_2-air

Figure 3.7 shows the temperature contours for H_2-air at 1:1, 1:8 and 1:128 scales. With a specific impulse that ranges between 2500 and 4000 seconds, the performance levels agree with previous experiments conducted in (**?**), which showed $F = 2200$N and $I_{sp} = 3600$s. The performance of the engine from geometric scales 1:1 to 1:64 sees no significant reduction for the hydrogen-fueled case. The performance metrics see a uniform drop across the first seven scales, as shown in Figures 3.5(a), 3.5(b), 3.6(a), and 3.6(b). The time required to mix and ignite the fuel is apparently adequate to develop a distinct diffusion flame as is seen in Figures 3.7(a) and 3.7(b). However, at the 1:128 scale there is no lifted diffusion flame (Figure 3.7(c)) as the turbulent mixing is significantly limited by the lack of fuel residence time (τ_r). A single molecule of hydrogen fuel continuously traveling at Mach 1 requires 3.4ms to move from the fuel injector to the nozzle exit in the 1:1 case, while it has just 0.027ms in the 1:128 case.

Figure 3.8 shows the H_2O mass fraction contours for H_2-air cases. It is observed that the cases 1:1, 1:2, 1:4, 1:8, 1:16, 1:32, and 1:64, all produce similar drop in product mass fraction exiting the nozzle, but 1:128 scale shows a significant reduction in product mass fraction at the nozzle exit. This can be attributed to the limited τ_r. Despite the large reduction in performance metrics in the 1:128 case, the ramjet is shown to still be able to maintain a positive F_N. This suggests the self-propelling capabilities of the

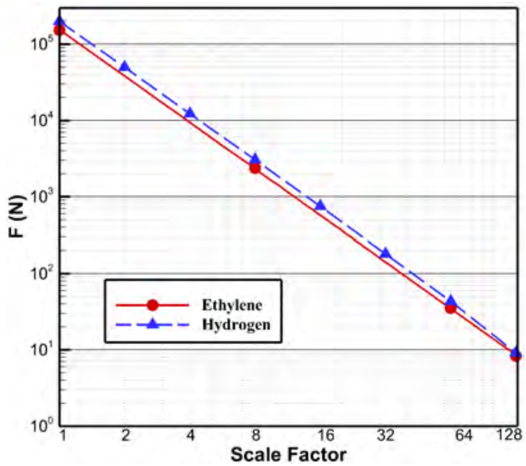

(a) Variation of F with scale.

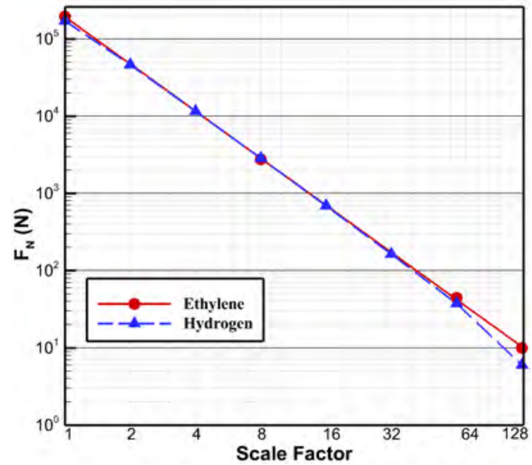

(b) Variation of F_N with scale.

Figure 3.5 Effects of geometric scale on F and F_N for H_2-air and C_2H_4-air.

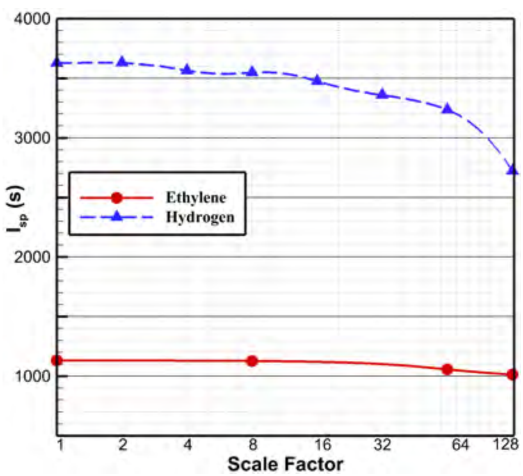

(a) Variation of I_{sp} with scale.

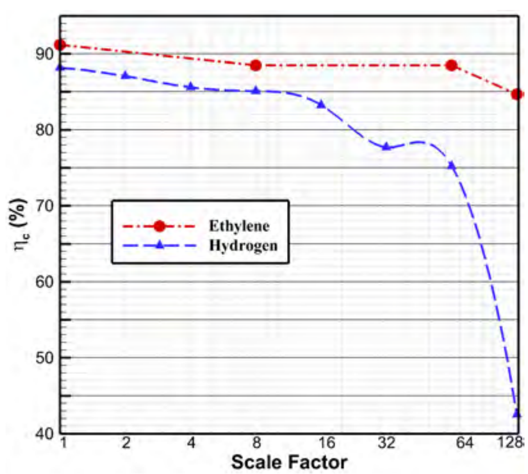

(b) Variation of η_c with scale.

Figure 3.6 Effects of geometric scale on I_{sp} and η_c for H_2-air and C_2H_4-air.

hydrogen-fueled ramjet flowpath is possibly scalable to the order of a few centimetres in length.

I_{sp} for the H_2-air ramjet flowpath (Figure 3.6(a)) shows a significant improvement versus SFRJ projectiles, which had values of 1111s (Dionisio and Stockenstrm, 2001).

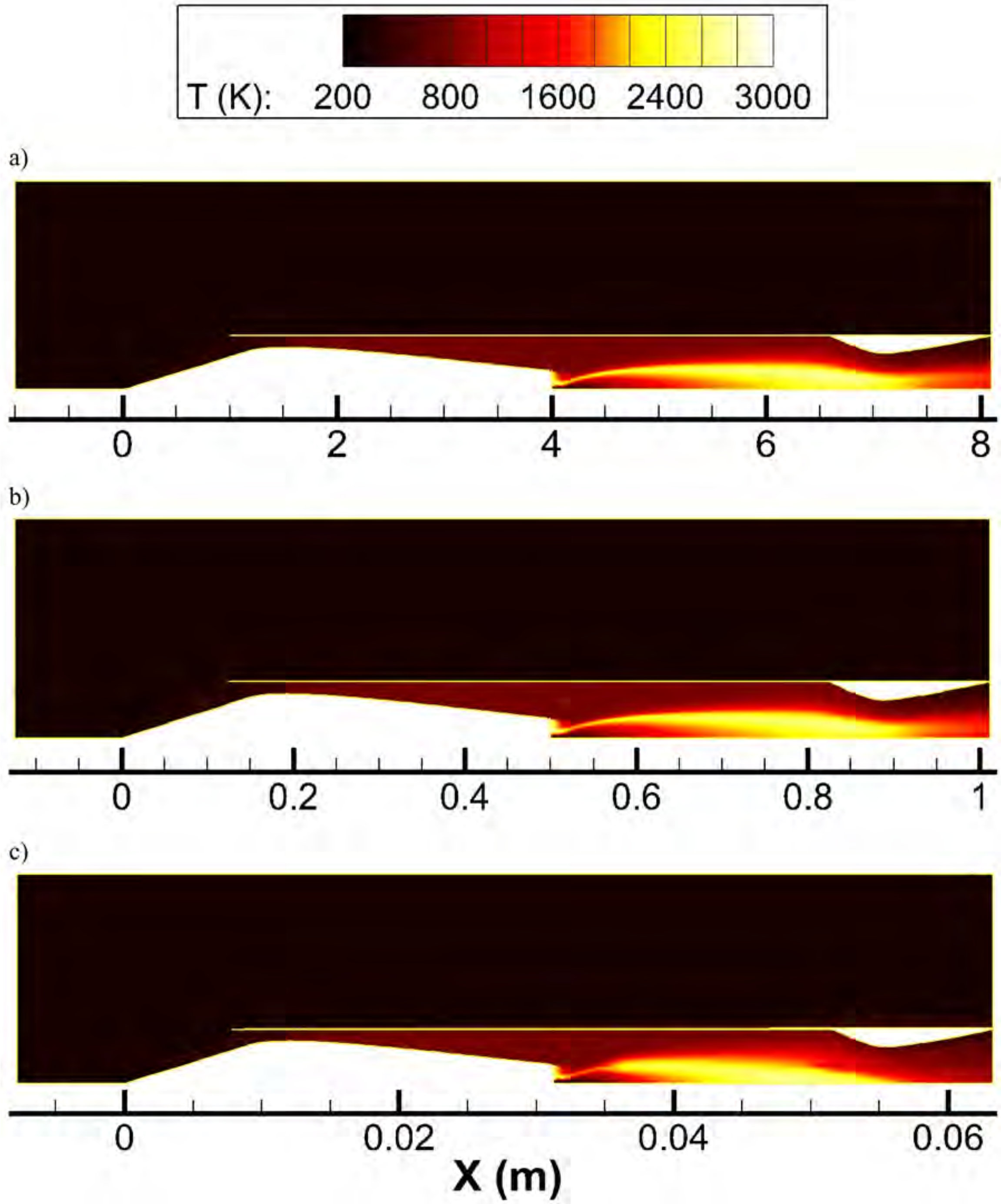

Figure 3.7 Temperature Contours for H_2-air reaction, a) Full-scale baseline, b) 1:8 scale, c) 1:128 scale

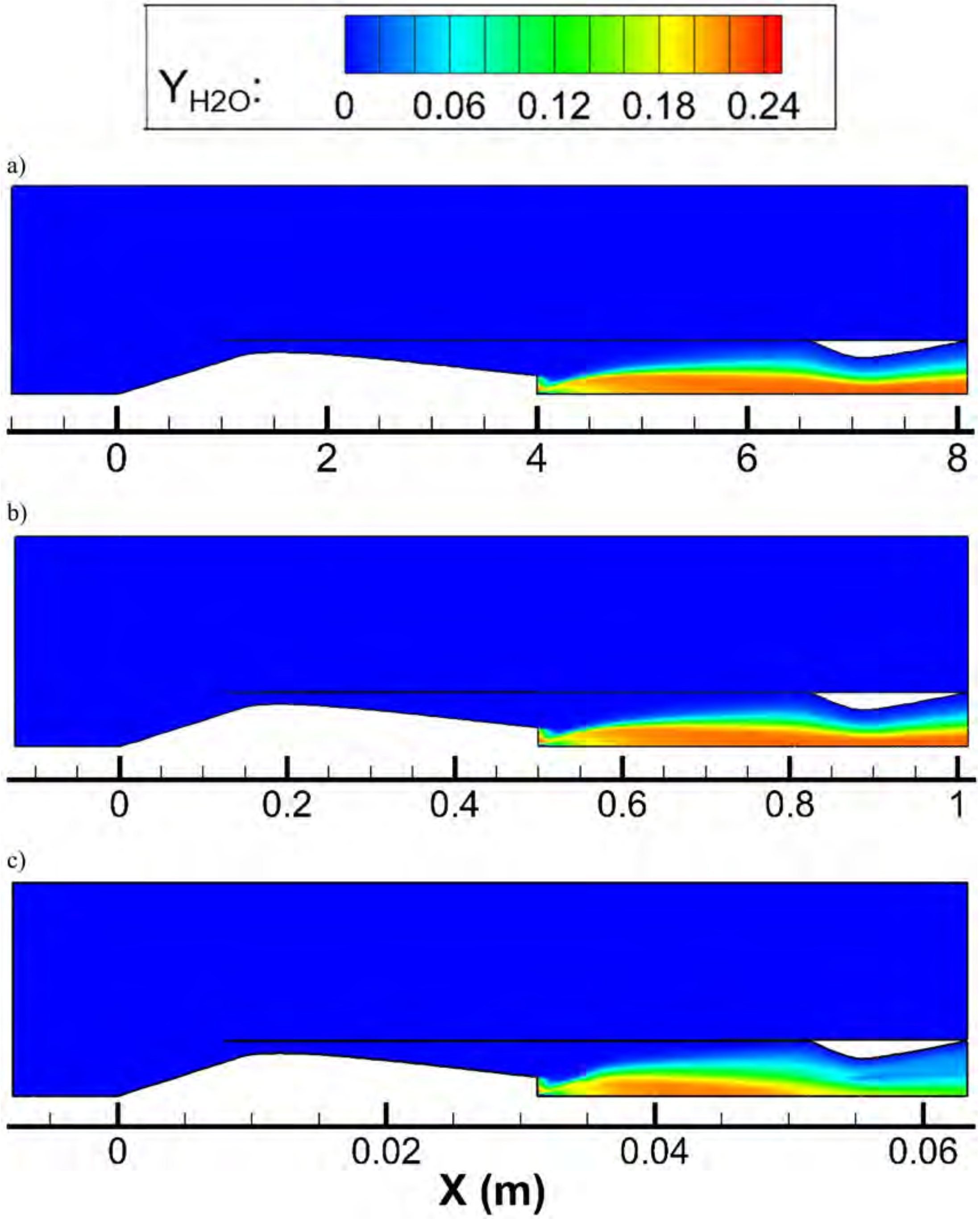

Figure 3.8 H_2O Mass Fraction Contours for H_2-air reaction, a) Full-scale baseline, b) 1:8 scale, c) 1:128 scale

The H_2-air case I_{sp} is also consistent with that measured in the experiment by Frolov et. al. (2017) with $\phi = 0.25$. The monotonic decrease in η_c and I_{sp} follow very similar trends, drawing a relation of the ramjet performance to its combustion efficiency. Similarly, F and F_N follow similar trends and remain positive even at the smallest scales, implying the hydrogen-fueled ramjet self-propelling capabilities are scalable to the orders of six centimetres in length. However, there are storage and injection limitations at these scales. Hydrogen requires enormous pressure for storage which is a logistical challenge when integrating the ramjet into a bullet shape of a sniper caliber.

3.3.2 C_2H_4-air

It was observed that the combustor inflow stagnation temperature is insufficient for auto-ignition of C_2H_4 at Mach 3 freestream flow. Note that the activation temperature for the C_2H_4-air reaction is 15,098K, almost five times higher than that of H_2-air (3726K). An increase to Mach 3.5 increased the combustor stagnation temperature sufficiently beyond the auto-ignition temperature of the fuel-air mixture. By increasing the fresstream velocity, overspeeding the engine also offers an additional measure to prevent engine unstart (Veillard et al., 2008).

Scaling effects for ethylene fuel shows a distinct lifted diffusion flame across every scale from 1:1 to 1:128, as shown in Figure 3.9. This is in contrast to the hydrogen cases, and the difference is attributed to a four-fold increase in τ_r for the fuel, based on the reduced speed of sound of the injected fuel, as well as the increase in stagnation temperature at Mach 3.5. Contours of mass fraction of CO_2 are shown in Figure 3.10, and products leaving the domain are also more consistent across the geometric scales than for H_2-air at Mach 3. The scale effects for C_2H_4-air at $\phi = 0.2$ are minimal, compared to that of H_2-air. I_{sp} at every scale shows results close to the 1111s in the SFRJ experiment by

Dionisio and Stockenstrm (2001). The performance metrics in Figures 3.5(a) 3.5(b) 3.6(a) and 3.6(b) suggest that small scale ramjet projectiles can potentially be developed using C_2H_4 fuel.

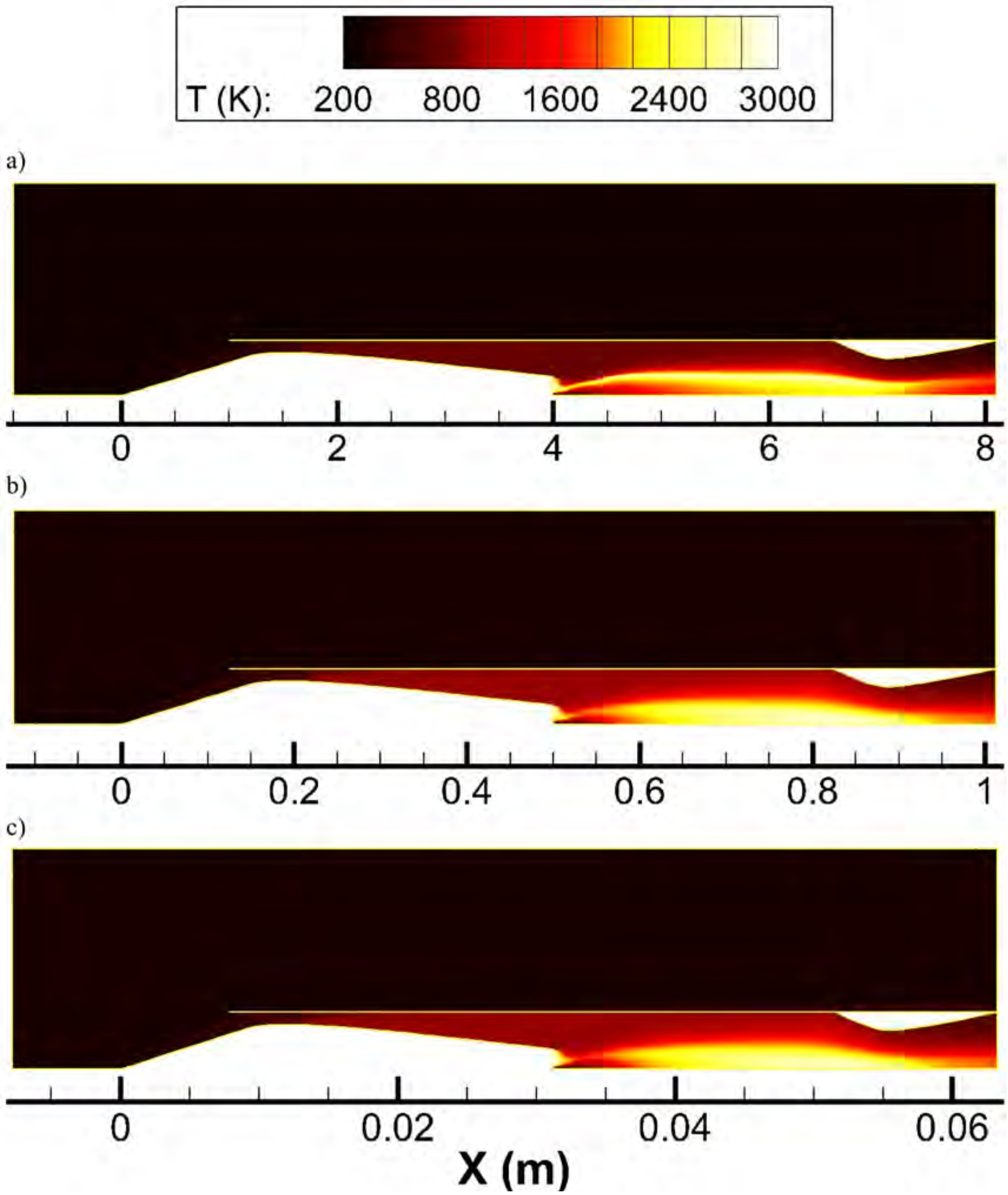

Figure 3.9 Temperature Contours for C_2H_4-air reaction, a) Full-scale baseline, b) 1:8 scale, c) 1:128 scale

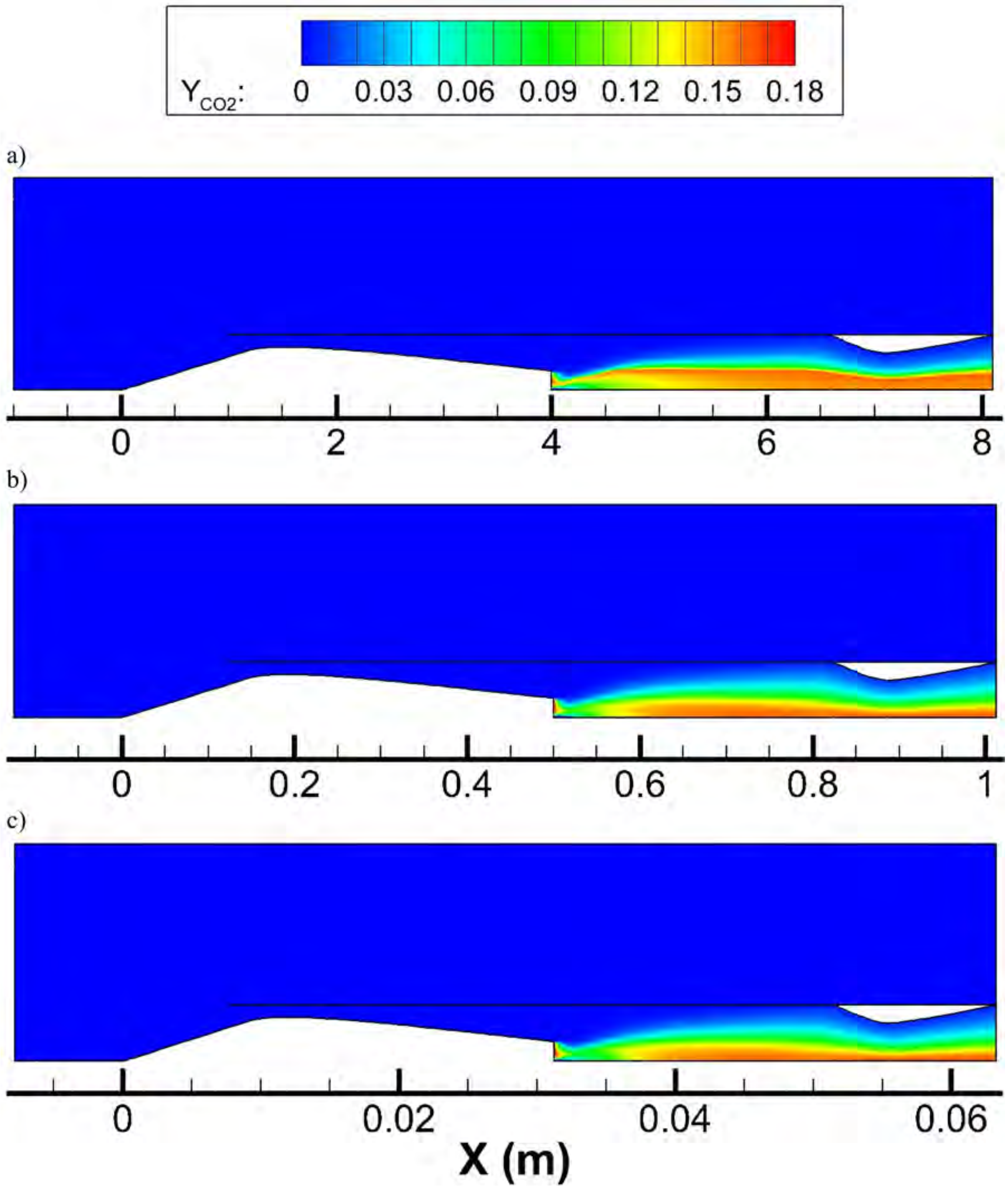

Figure 3.10 CO_2 Mass Fraction Contours for C_2H_4-air reaction, a) Full-scale baseline, b) 1:8 scale, c) 1:128 scale

3.3.3 Effects of Geometric Scale on Turbulent Transition

Turbulence plays an important role in initiating mixing and auto-ignition. The shear layer formed by sonic injected fuel and subsonic air enhances turbulent mixing. The EDM chemical interaction model is heavily reliant on this turbulent shear layer. To investigate the level of turbulence near the injection region, maximum turbulent kinetic energy (k or TKE) near the injector region is plotted to show effect of geometric scale in Figure 3.11(a). It is apparent that a reduction in geometric scale does not reduce peak levels of turbulence near the injection port, and hence does not cause lack of combustion at the smallest geometric scales. The relative lack of turbulence in C_2H_4-air compared to H_2-air must be noted in Figure 3.11(a). Sonic ethylene enters the combustor at a velocity 332 m/s, which is approximately four times lower than that of sonic hydrogen, which enters at 1206 m/s. This reduction in velocity results in smaller strain rates and appears to be the primary cause of reduced turbulence levels produced in the C_2H_4-air interaction. An in-depth study of small scale injectors is expected to show realistic levels of inflow turbulent data.

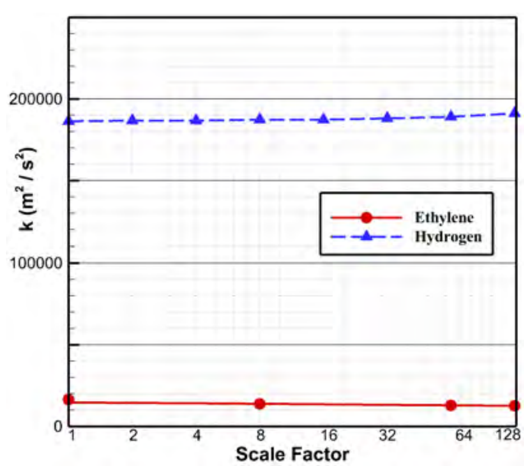

(a) Variation of k with scale.

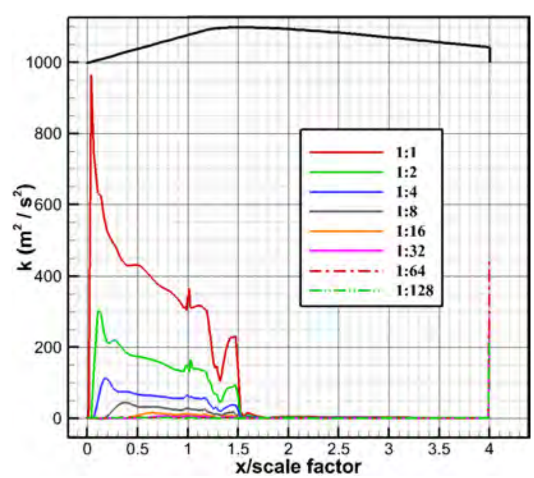

(b) Distribution of k along diffuser walls at different scales.

Figure 3.11 Effects of geometric scale on turbulence levels.

Turbulent kinetic energy (k) along the intake and diffuser walls up to the entrance of the combustor for all geometric scales is shown in Figure 3.11(b). A common trend is the re-laminarization of the flow downstream of the normal shock just downstream of the throat (x/scale factor = 1.5), across all geometric scales. The flow is laminar throughout along the walls from 1:16 to 1:128 scales. The boundary layer is tripped again only at the entrance of the combustor, as observed by the spike in *k* at the combustor entrance at x/scale factor = 4 in Figure 3.11(b). The re-circulation zone at the diffuser exit and combustor entrance acts as a flameholder.

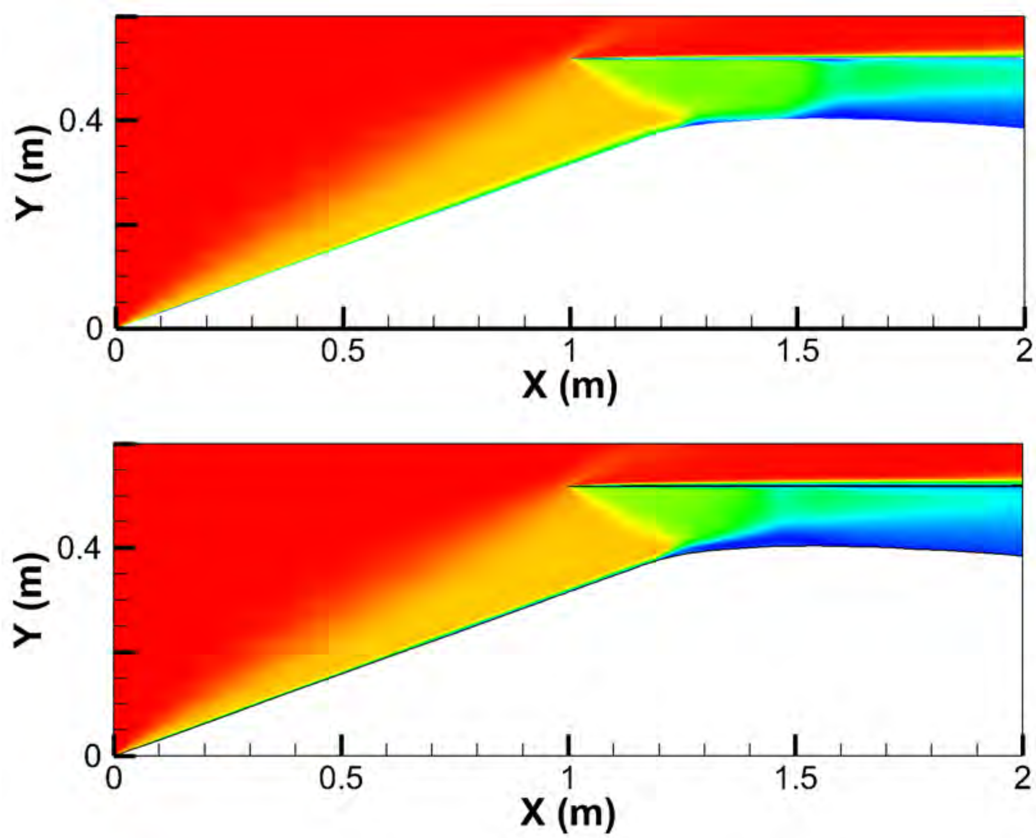

Figure 3.12 Shock-Boundary Layer Interaction causing inlet unstart at 1:256 scale (bottom), compared to the started 1:128 scale (top)

The laminar nature of the flow at the geometric scales lower than 1:16 combined with the shock impingement off the cowl lip, causes flow separation at the inlet throat due to the laminar nature of the flow. Below the 1:128 scale, this effect becomes prominent and prevents critical mass flow from passing into the diffuser and combustor sections, leading to an inlet unstart, as shown in Figure 3.12 for Mach 3 H_2-air. The performance at the 1:256 scale is not evaluated due to this phenomenon. A high-fidelity LES simulation is recommended to observe the growth of the separation bubble at the inlet throat.

3.4 3-D Flowpath Analysis

The 3-D model should provide a more realistic representation of the ramjet combustion performance. As designed earlier, the model is setup as a 30-degree pie-section with a port injection aft on the diffuser rearward-facing step. More refined grid near the injection port is expected to more accurately model fuel-air mixing and combustion.

3.4.1 Sensitivity to Chemical Kinetics Model

The sensitivity of the flowpath performance to chemical kinetics models is evaluated in this subsection using three chemical approaches described in the Methodology chapter. Table 3.2 compares the values of F, I_{sp} and η_c at different levels of fuel inflow turbulence using the three different chemical interaction models. Figure 3.13 shows the temperature contours for the three kinetics models with fuel injected at $k = 1000\ m^2/s^2$. The laminar FR model produces the highest temperatures inside the combustor, as well as the highest I_{sp}. Raising the inflow Mach to 3.5 ensures that the stagnation temperature is well above the reaction activation temperature. The FR model takes time to ignite, but once ignited, the flame propagates upstream and produces a distinct diffusion flame.

The EDM model ignites the earliest, but it produces the lowest temperatures in the combustor as well as the lowest I_{sp} and lowest efficiency of all three models. Turbulence

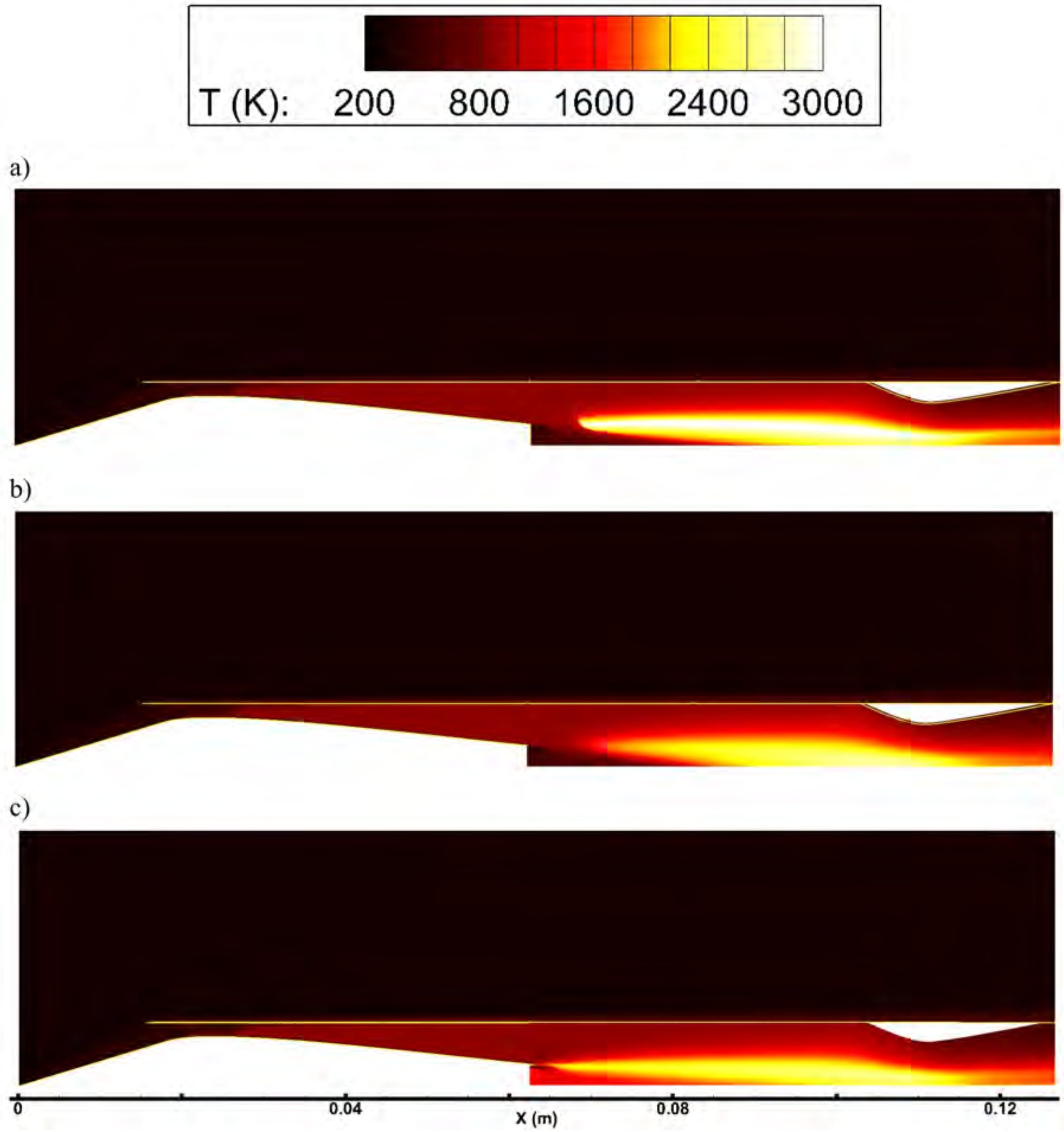

Figure 3.13 Temperature contours of (a) FR, (b) FR-EDM, (c) EDM

is limited further downstream of the injector and limits the overall performance of the ramjet flowpath.

The FR-EDM model results suggest that the chemical reaction rates are smaller than the turbulent mixing and reaction rates near the flameholder, suppressing ignition in that

Table 3.2

Comparison of performance metrics for different chemical interaction models

Reaction Model	Fuel inflow $k(m^2/s^2)$	I_{sp} (s)	F (N)	η_c (%)
FR	1000	966.59	36.001	91.22%
EDM	1000	811.78	30.24	83.63 %
	100	811.86	30.24	83.56%
	1	796.58	29.67	82.64%
FR-EDM	1000	965.99	35.98	89.89%
	100	963.6	35.89	89.89%

region. The flow ignites further downstream, similar to the FR model, but never produces as high a temperature as the FR model. This suggests that the turbulent mixing and reaction rates are limiting further downstream in the combustor, similar to the EDM model.

To visualize the different reactions taking place within the combustor, Figures 3.14 and 3.15 show the chemical reaction rates and turbulent mixing reaction rates, respectively, for the FR-EDM model with inflow $k = 1000\ m^2/s^2$. The contours further suggest that the turbulent reaction reactions are larger in the flameholder region but tend to dissipate further downstream of the combustor, at which point the chemical reaction rates are larger.

The combustion efficiency of each chemical kinetics model is shown in Figure 3.16. Mass flow-weighted average of CO_2 mass fraction is integrated at 100 streamwise locations from the combustor entrance to the nozzle exit, and η_c is calculated using Equation 2.7. All of the models predict good combustion efficiency between 80% and 92% The FR model performs the best at Mach 3.5. The EDM model performs least favorably, with a 9% lower η_c than the FR and 6% lower than the FR-EDM model. The FR-EDM model shows a change of < 2% when compared to the FR model.

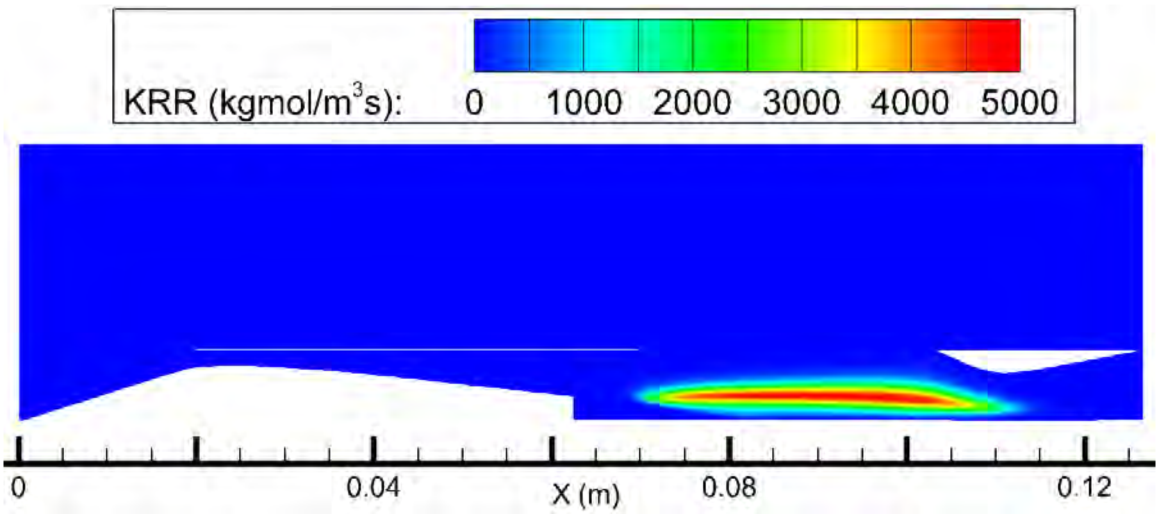

Figure 3.14 Kinetic Reaction Rate (KRR) for the FR-EDM model.

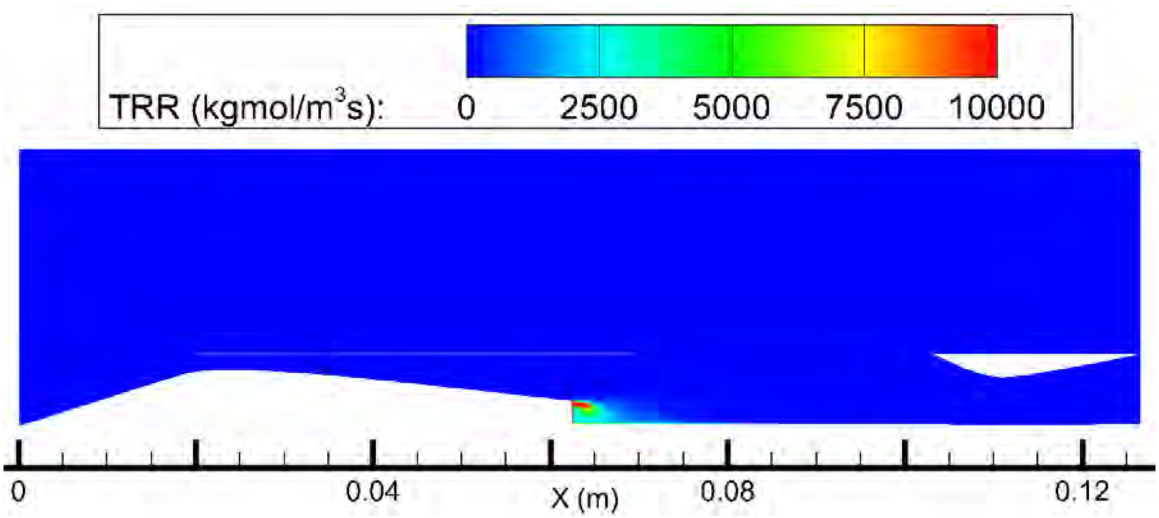

Figure 3.15 Turbulent mixing-limited reaction rate (TRR) for the FR-EDM model.

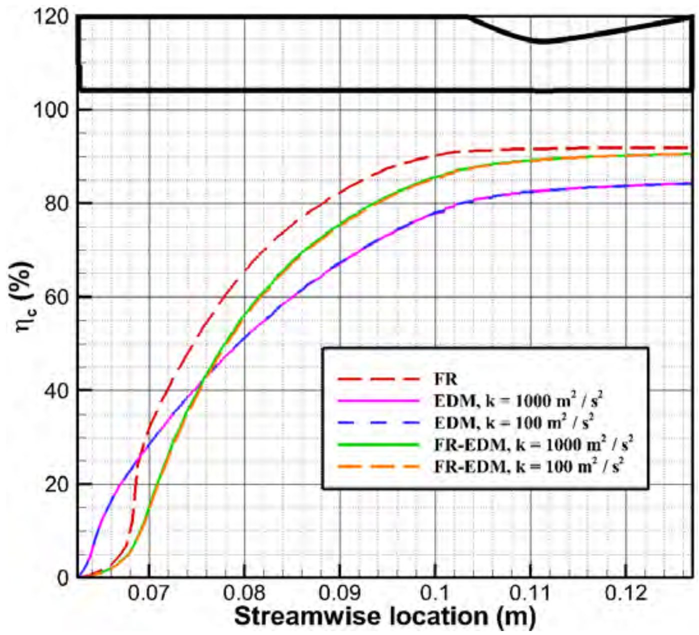

Figure 3.16 Combustion efficiency for different chemical interaction models at the 1:64 scale.

3.4.2 Sensitivity to Fuel Inflow *k*

Based on the evaluation of CFD in the fuel injector flowpath in Section 3.2, $100 \leq k \leq 1000\ m^2/s^2$ is a realistic range of values for k at injector exit plane. The EDM and FR-EDM models are reliant on levels of turbulence for combustion. Contours of Y_{CO_2} are shown in Figures 3.17 and 3.18 for the EDM and FR-EDM interaction models, respectively, at fuel inflow k of 100 m^2/s^2 and 1000 m^2/s^2, and ω = 1.0E+07 s^{-1}. Results demonstrate negligible sensitivity when comparing the same chemical interaction models, with $< 1\%$ change in the performance metrics, as shown in Figure 3.16 and Table 3.2. However, with inflow $k = 1\ m^2/s^2$, there was a significant reduction in performance using the EDM model as shown in Table 3.2. This indicates that fuel injection requires a higher level of inflow k ($\geq 100 m^2/s^2$) for sustained performance levels. The flowpath performance is essentially independent of magnitude of inflow k since the shear layer generates sufficient turbulence for mixing and ignition.

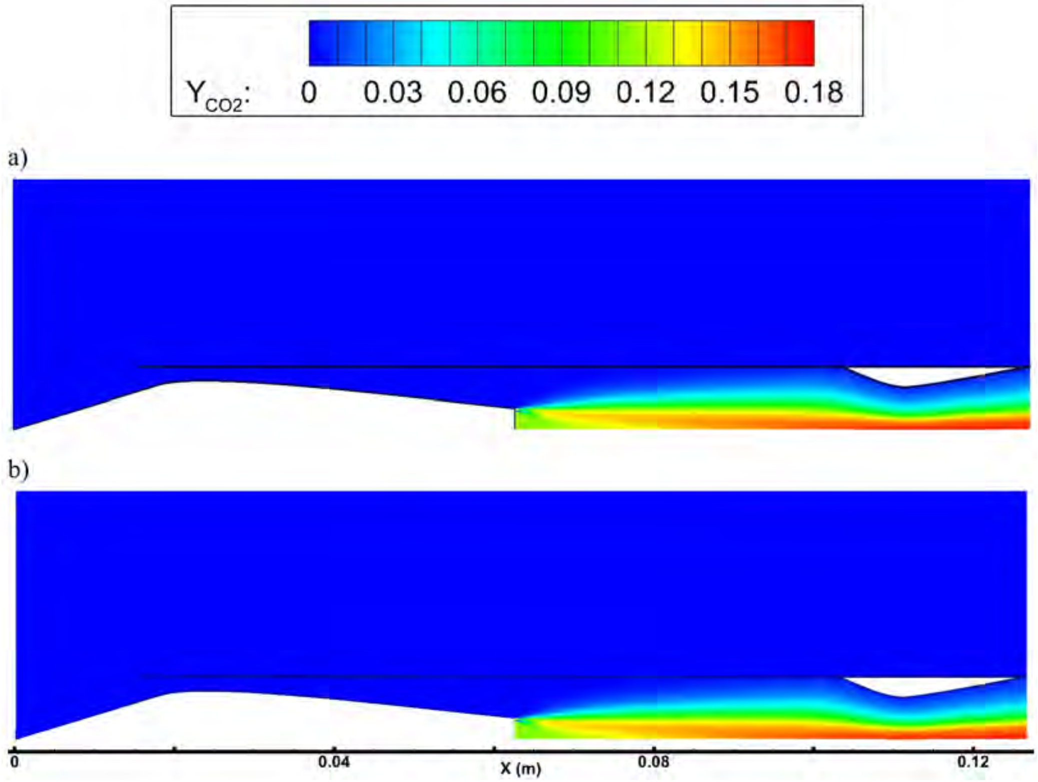

Figure 3.17 Contours of carbon-dioxide for EDM model. (a) $k = 100\ m^2/s^2$, (b) $k = 1000\ m^2/s^2$

Figure 3.19 shows the growth and eventual dissipation of k downstream of the injector port. The shear layer between fuel jet and recirculating air increases k to nearly 10 times its injection value before eventually dissipating, raising the turbulent mixing and reaction rates well above the chemical and reaction rates, which was apparent in Figures 3.14 and 3.15.

3.4.3 High-fidelity CFD calculations

The smallest turbulent scale in any flow is known as the Kolmogorov microscale (η_κ). At these turbulent scales, k dissipates into heat. For numerical dissipation of k, the

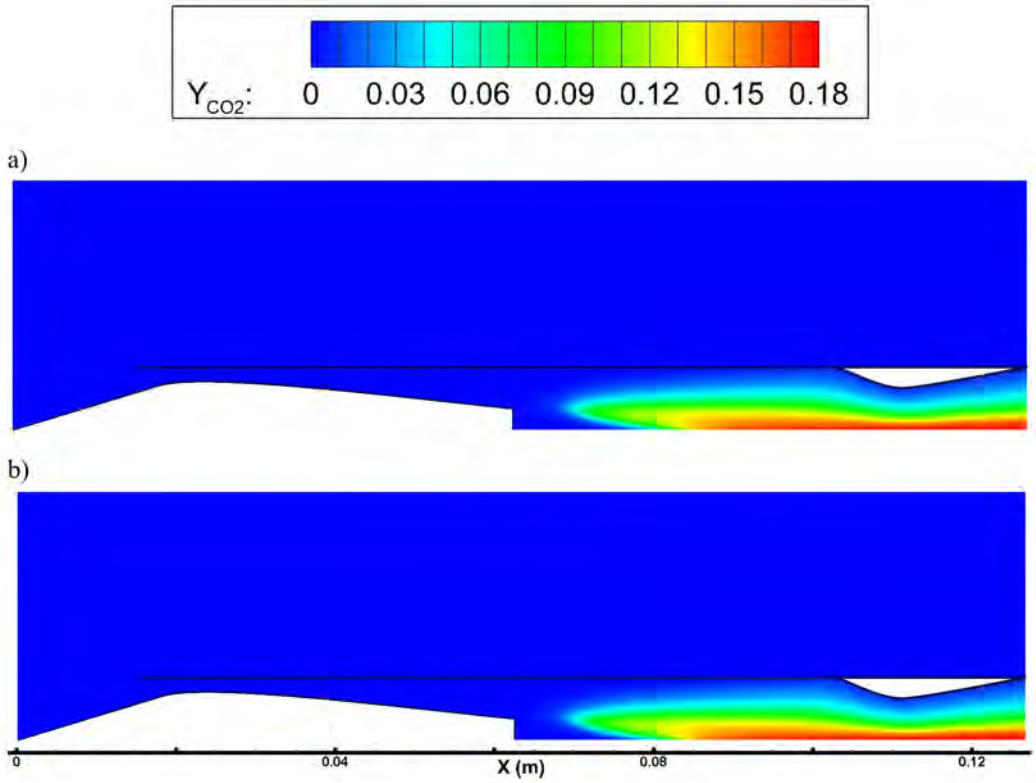

Figure 3.18 Contours of carbon-dioxide for FR-EDM model. (a) $k = 100\ m^2/s^2$, (b) $k = 1000\ m^2/s^2$

Figure 3.19 Transport of k within the injection for inflow $k = 1000\ m^2/s^2$

η_κ field can be calculated using Equation 3.2, where ε is the rate of dissipation of k, and ν is the kinematic viscosity of air. The RANS model solves for k and ω turbulence variables and the relation in Equation 3.3 is used to calculate ε, with $C_\mu = 0.09$. Figure 3.20 shows

XY and YZ slices of η_κ at every cell in the combustor and nozzle sections. An isotropic grid size of 1.4E-07m would resolve the smallest eddies near the injector in the 1:64 scale. Figure 3.21 shows the calculated Kolmogorov scale vs scale factor for every geometric scale using the 2-D results.

$$\eta_\kappa = \left(\frac{\nu^3}{\varepsilon}\right)^{\frac{1}{4}} \tag{3.2}$$

$$\varepsilon = C_\mu k \omega \tag{3.3}$$

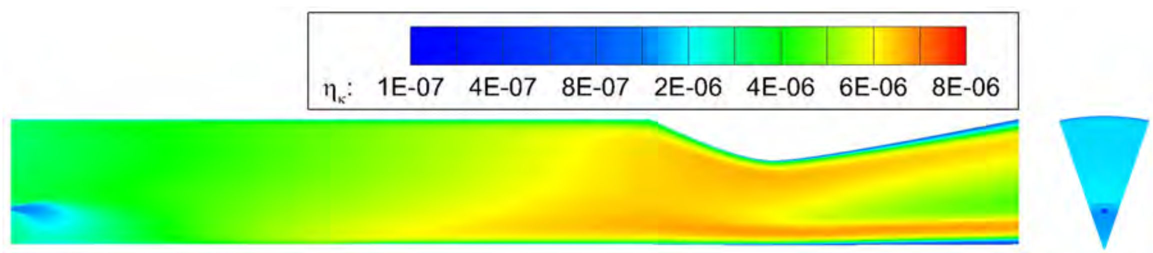

Figure 3.20 Range of Kolmogorov scales (in m) in the domain for 1:64 scale using C_2H_4 fuel.

An approximation of the grid size required for a DNS calculation for the 1:64 scale at Mach 3.5, can be calculated. The equations from (Zikanov, 2010) are used to calculate number of grid points. First, the turbulent Reynolds number is determined using Equation 3.4, where u' is the root-mean-square free-stream velocity, calculated using Equation 3.5, and L is the overall length of the computational domain. The number of grid points, N, is then estimated using the Kolmogorov value using Equation 3.6. The grid size required to solve for the flow using DNS is 6.13E+15 cells, which is intractable.

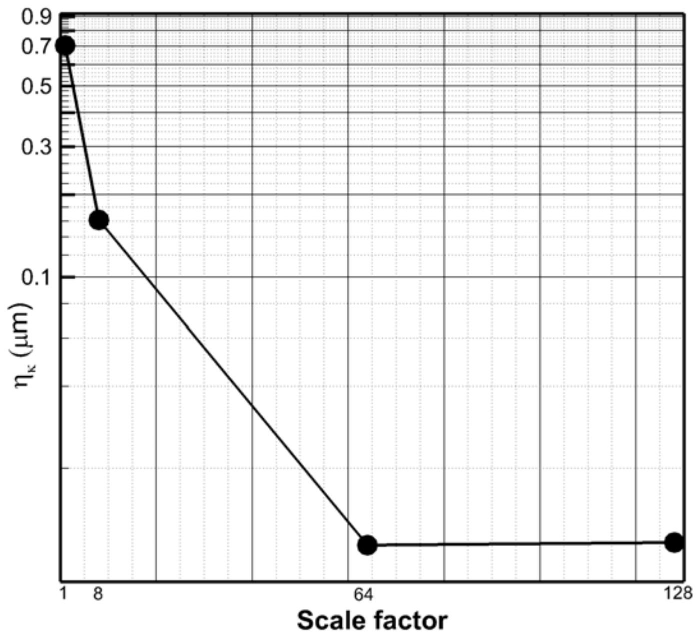

Figure 3.21 Range of Kolmogorov scales for all geometric scales using C_2H_4 fuel.

$$Re_{turb} = \frac{u'L}{\nu} \tag{3.4}$$

$$u' = (\varepsilon L)^{\frac{1}{3}} \tag{3.5}$$

$$N^3 = Re_{turb}^{2.25} \tag{3.6}$$

Rather than a DNS, an LES numerical analysis to resolve the small scale eddies near the injection port and transport of k within the combustor will be useful in evaluating the ramjet performance.

4. Integrated Design Considerations

Ferguson (2003) developed a structurally robust projectile using 304 stainless steel and 7075 aluminum alloy. It was shown experimentally that the ramjet structure could handle aerodynamic loading at $M_\infty = 4.0$ at an overall length of 7 inches. However, only non-reacting flows were tested. A CAD model of the ramjet assembly and the fully assembled ramjet model are shown in Figures 4.1 and 4.2, respectively (Ferguson, 2003).

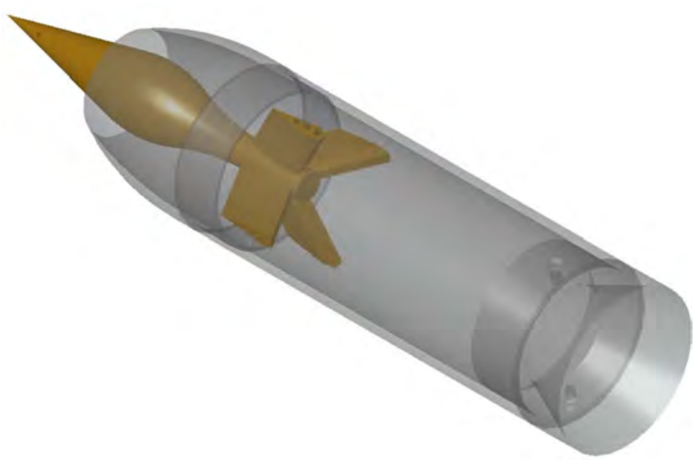

Figure 4.1 Assembled CAD model showing all parts of the ramjet.

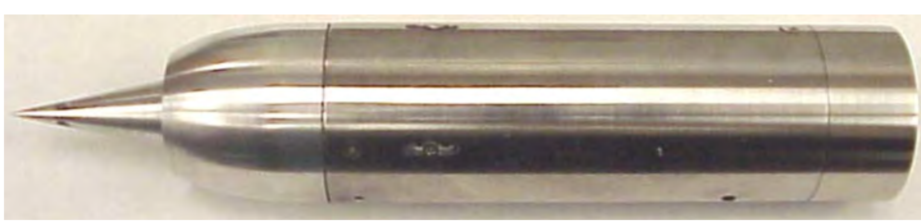

Figure 4.2 Fully assembled ramjet.

The current work suggests that a ramjet propulsion system will be thermally efficient at geometric scales on the order of a few centimetres in length. To determine if the ramjet flowpath can be practically integrated into a munition, the outer casing drag ($F_{drag,casing}$)

of the munition is evaluated using Equation 4.1 and compared to the available positive F_N of the ramjet flowpath at Mach 3.5. Figure 4.3 shows the allowable outer diameter of a munition casing, D (normalized by munition diameter, D_{ram}), versus geometric scale. The plot indicates that the ramjet flowpath can be integrated into a munition casing with an annular diameter 1.5 times greater than the diameter of the flowpath. The casing provides structural integrity as well as room for pressurized fuel storage. Since the ramjet flowpath accounts for the overall internal drag, the external drag is evaluated for the annular ramjet casing, shown in gray in Figure 4.4. The inviscid drag coefficient for the outer casing is evaluated using Equation 4.2 by integrating the axial component of the pressure forces over the annular casing, based on oblique-shock theory. The value of $C_{D,casing}$ is approximately 0.06.

$$F_{drag,casing} = F_N = \frac{1}{2}\rho u_\infty^2 S_{casing} C_{D,casing} \tag{4.1}$$

$$C_{D,casing} = \frac{F_{drag,casing}}{q_\infty S_{casing}} \tag{4.2}$$

A first order calculation for flight time can be made. At the 1:64 scale, the volume of pressurized C_2H_4 stored at 500 bar is equal to 21 mL. Making an assumption that 80% of the volume is used for fuel storage, the total mass of C_2H_4 stored is 11g. At a constant fuel injection ϕ of 0.2, the self-propelling capability of the munition lasts as long as 3.23s. At a constant flight velocity of M_∞ = 3.5 at sea-level, the extended range of the ramjet-powered munition is 3.9km.

The flowpath and casing shape at the 1:64 scale is compared to the G7 ballistic projectile's shape (Litz, 2016) in Figure 4.5. The G7 profile is a standard for long-range

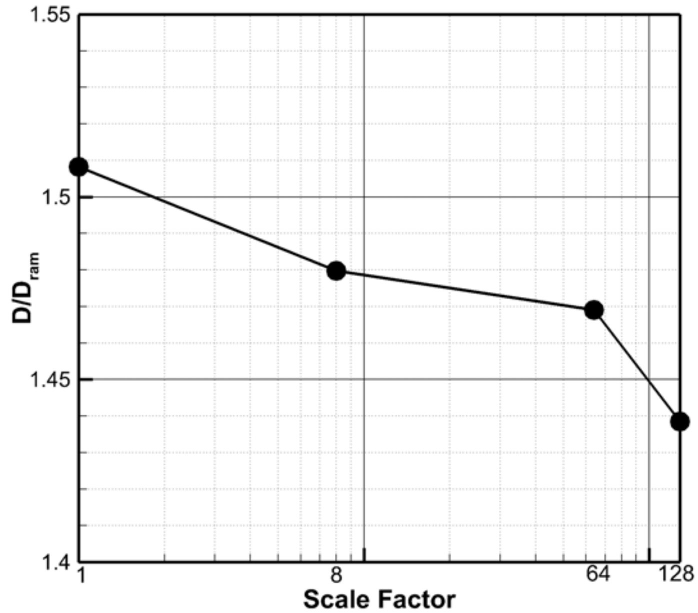

Figure 4.3 Ratio of diameters for different scales

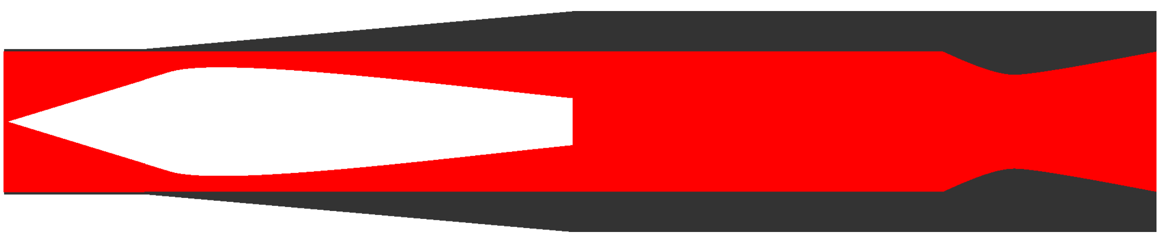

Figure 4.4 Ramjet flowpath (red) integrated within an outer munition casing (grey).

projectiles and is used here to compare with the diameter-to-length ratio of the ramjet-powered munition shown in Figure 4.4. It is observed that the overall munition diameter is significantly lower than the G7, implying that the outer casing diameter for the flowpath can be further increased to accommodate a larger volume of fuel, increasing overall range and flight time of the proposed flowpath. The latter would likely require operation at a slightly large ϕ to compensate for this drag increase.

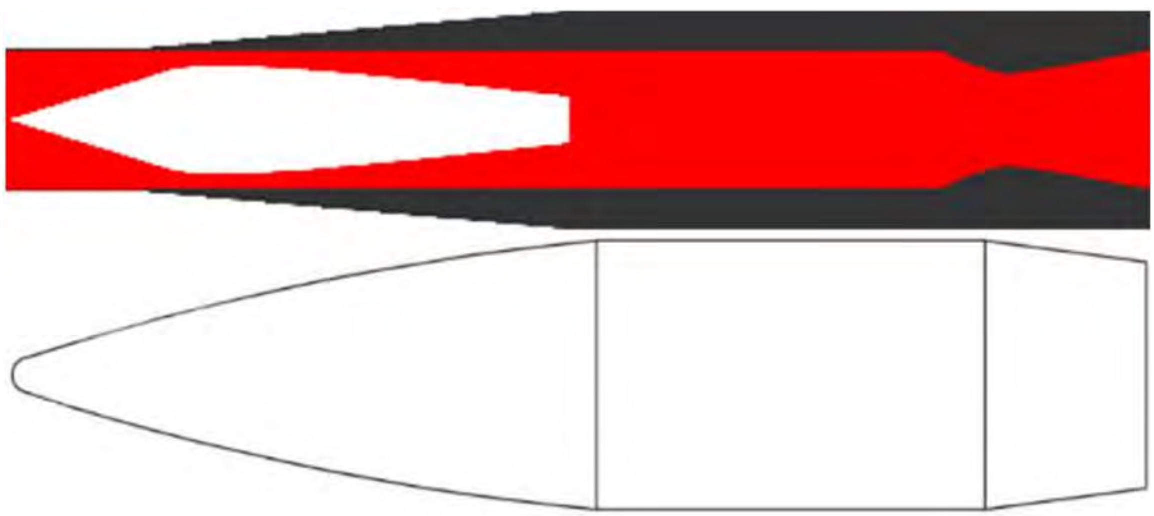

Figure 4.5 Current ramjet-powered munition (top) compared to standard G7 projectile (bottom).

5. Conclusion

A preliminary numerical investigation was performed to determine the effects of geometric scale on the performance of a simplified 2-D axisymmetric ramjet flowpath using two different fuels: H_2 and C_2H_4. It was found that the ramjet flowpath could be reduced to a size as small as nearly 5cm long, without a significant loss in performance metrics (i.e. F, I_{sp}, η_c) for either fuel. The freestream Mach number (M_∞) was maintained at 3.0 for H_2, but increased to 3.5 for C_2H_4 so that the fuel could auto-ignite. Ramjet intake unstart due to shock-boundary layer interaction of the laminar flow along the conical centerbody was a limiting factor in the geometric scaling process, restricting the scale factor to no smaller than 1:128.

The 2-D grid was extended to a 3-D 30° pie-section, and investigated for performance limitations at $M_\infty = 3.5$ for the 1:64 scale using C_2H_4 fuel. It was observed that extending the grid to 3-D did not significantly reduce performance. The sensitivity to different chemical interaction models was also investigated using FR, EDM, and FR-EDM models. All three models produced η_c between 80-92% and I_{sp} between 800-1000s. Sensitivity of the FR-EDM and EDM chemical interaction models to fuel inflow k was shown to be negligible for inflow k between 1-1000 m^2/s^2. The shear layer within the injected fuel plume generates enough turbulence to ignite the fuel and produce a sustained diffusion flame. The numerical results, combined with the first order calculations for range and time, suggests that there is potential for self-propelling small-scale ramjet projectiles.

REFERENCES

Anderson, J. D. (1982). *Modern Compressible Flow, with Historical Perspective*. McGraw-Hill.

ANSYS-Inc. (2019a). *ANSYS Fluent Theory Guide*.

ANSYS-Inc. (2019b). *ANSYS Fluent User's Guide*.

Borghi, M. R., Engblom, W. A., and Georgiadis, N. J. (2014). Evaluation of Mixing-Limited Quasi-Global Wind-US Model for HIFiRE 2 Flowpath. National Harbor, Maryland. 52^{nd} Aerospace Sciences Meeting, AIAA SciTech Forum.

Burrows, M. C. and Kurkov, A. P. (1971). Supersonic Combustion of Hydrogen in a Vitiated Air Stream Using Stepped-Wall Injection. Number 71-721, Salt Lake City, Utah. AIAA/SAE 7^{th} Propulsion Joint Specialist Conference.

Chen, S., Chue, R. S. M., Schlter, J., Nguyen, T. T. Q., and Yu, S. C. M. (2015). Numerical Investigation of a Trapped Vortex Miniature Ramjet Combustor. *Journal of Propulsion and Power*, 31(3):872–882.

Courant, R., Friedrichs, K., and Lewy, H. (1956). On the Partial Difference Equations of Mathematical Physics. *AEC Research and Development Report*.

Dionisio, F. and Stockenstrm, A. (2001). Aerodynamic Wind-Tunnel Test of a Ramjet Projectile. Switzerland. 19^{th} International Symposium of Ballistics.

Duke-Robotics (2017). TIKAD Drone. https://dukeroboticsys.com/#product.

Edwards, J. R., Boles, J. A., and Baurle, R. A. (2010). LES/RANS Simulation of a Supersonic Reacting Wall Jet. Orlando, Florida. 48^{th} AIAA Aerospace Sciences Meeting.

Edwards, J. R. and Fulton, J. A. (2015). Development of a RANS and LES/RANS Flow Solver for High-Speed Engine Flowpath Simulations. Glasgow, Scotland. 20^{th} AIAA International Space Planes and Hypersonic Systems and Technologies Conference.

Engblom, W., Frate, F., and Nelson, C. (2005). Progress in Validation of Wind-US for Ramjet/Scramjet Combustion. Reno, Nevada. 43^{rd} AIAA Aerospace Sciences Meeting and Exhibit.

Ferguson, K. M. (2003). *Design and Cold Flow Evaluation of a Miniature Mach 4 Ramjet*. Master's Thesis, Naval Postgraduate School, Monterey, California.

Frauholz, S.and Reinartz, B. U., Mller, S., and Behr, M. (2015). Transition Prediction for Scramjets Using $\gamma - Re_{\theta t}$ Model Coupled to Two Turbulence Models. *Journal of Propulsion and Power*, 31(5):1404-1422.

Frolov, S. M., Zvegintsev, V. I., Ivanov, V. S., Aksenov, V. S., Shamshin, I. O., Vnuchkov, D. A., Nalivaichenko, D. G., Berlin, A. A., , and Fomin, V. M. (2017). Tests of the Hydrogen-Fueled Detonation Ramjet Model in a Wind Tunnel with Thrust Measurements. volume 1893. AIP Conference Proceedings.

Georgiadis, N., Mankbadi, M., and Vyas, M. (2014). Turbulence Model Effects on RANS Simulations of the HIFiRE Flight 2 Ground Test Configurations. National Harbor, Maryland. 52^{nd} Aerospace Sciences Meeting, AIAA SciTech Forum.

Georgiadis, N., Yoder, D., Vyas, M., and Engblom, W. (2011). Status of Turbulence Modeling for Hypersonic Propulsion Flowpaths. San Diego, California. 47^{th} AIAA/ASME/SAE/ASEE Joint Propulsion Conference Exhibit.

Gilreath, H. E. (1990). The Beginning of Hypersonic Ramjet Research at APL. *Johns Hopkins APL Technical Digest*, 11:pp. 319–335.

Granizo, J. F., Gudmundsson, S., and Engblom, W. A. (2017). Effect of Slot Span on Wing Performance. Denver, Colorado. AIAA Aviation Forum.

Judson, J. (June 2018). Nammo rolls out its extreme range artillery. https://www.defensenews.com/digital-show-dailies/eurosatory/2018/06/14/nammo-rolls-out-its-extreme-range-artillery/.

Langtry, R. B. and Menter, F. R. (2009). Correlation-Based Transition Modeling for Unstructured Parallelized Computational Fluid Dynamics Codes. *AIAA Journal*, 47:pp. 2894–2906.

Liou, M. S. and Steffen Jr., C. J. (1993). A New Flux Splitting Scheme. *Journal of Computational Physics*, 107:23–39.

Liou, W. and Shih, T.-H. (1996). Transonic Turbulent Flow Predictions With New Two-Equation Turbulence Models. *NASA Contractor Report*, (198444).

Litz, B. (2016). Aerodynamic Drag Modeling for Ballistics. *Applied Ballistics*.

Magnussen, B. (1981). On the Structure of Turbulence and a Generalized Eddy Dissipation Concept for Chemical Reaction in Turbulent Flow. *19th AIAA Meeting*.

Magnussen, B. and Hjertager, B. (1977). On Mathematical Models of Turbulent Combustion with Special Emphasis on Soot Formation and Combustion. *Proceedings of 16th Symposium (International) on Combustion*, 16:719-729.

McBride, B. J., Gordon, S., and Reno, M. A. (1993). Coefficients for Calculating Thermodynamic and Transport Properties of Individual Species. NASA Technical Memorandum 4513.

Menter, F. R. (1994). Two-Equation Eddy-Viscosity Turbulence Models for Engineering Applications. *AIAA Journal*, 32:pp. 1598–1605.

Menter, F. R., Langtry, R., and Volker, S. (2006). Transition Modelling for General Purpose CFD Codes. *Flow, Turbulence and Combustion*, 77(1):pp. 277–303.

Minotti, A. and Bruno, C. (2011). LES of a CH4/air Mesocombustor at 3 atm: EDC and Laminar-rate models. Orlando, Florida. 49^{th} AIAA Aerospace Sciences Meeting.

Ouellette, N. T. (May, 2012). Turbulence in Two Dimensions. *Physics Today*, 65(5).

Raytheon (2015). Pike Munitions. https://www.raytheon.com/capabilities/products/pike.

Stockenstrm, A. (2001). Numerical Model for Analysis and Specification of a Ramjet Propelled Artillery Projectile. Switzerland. 19^{th} International Symposium of Ballistics.

Sutherland, W. (1893). The viscosity of gases and molecular force. *The London, Edinburgh, and Dublin Philosophical Magazine and Journal of Science*, 36(223):507–531.

USArmy (2017). Army Research Laboratory Broad Agency Announcement for Basic and Applied Scientific Research. Number W911NF17S0003, Aberdeen Proving Ground. United States Army Contracting Command.

Veillard, X., Tahir, R., Timofeev, E., and Molder, S. (2008). Limiting Contractions for Starting Simple Ramp-Type Scramjet Intakes with Overboard Spillage. *Journal of Propulsion and Power*, 24(5):1042–1049.

Vyas, M., Engblom, W., Georgiadis, N., Trefny, C., and Bhagwandin, V. (2012). Numerical Simulation of Vitiation Effects on a Hydrogen-Fueled Dual-Mode Scramjet. Orlando, Florida. 48^{th} AIAA Aerospace Sciences Meeting Including the New Horizons Forum and Aerospace Exposition.

Willems, J., Engblom, W., and Wurts, J. (2018). Verification, Validation, and Application of Shear Stress Transport Transitional Model to a R/C Aircraft. Kissimmee, Florida. 2018 AIAA Aerospace Sciences Meeting.

You, Y., Luedeke, H., Eggers, T., and Hannemann, K. (2012). Application of the $\gamma - Re_{\theta t}$ Transition Model in High Speed Flows. Tours, France. 18^{th} AIAA/3AF International Space Planes and Hypersonic Systems and Technologies Conference.

Zikanov, O. (2010). *Essential Computational Fluid Dynamics*. John Wiley and Sons, Hoboken, New Jersey.